International Journal of
Extreme
Manufacturing

Preparation of single atom catalysts for high sensitive gas sensing

Xinxin He, Ping Guo, Xuyang An, Yuyang Li, Jiatai Chen, Xingyu Zhang, Lifeng Wang, Mingjin Dai, Chaoliang Tan, Jia Zhang

View online: https://doi.org/10.1088/2631–7990/ad3316

International Journal of Extreme Manufacturing

TOPICAL REVIEW • OPEN ACCESS

Preparation of single atom catalysts for high sensitive gas sensing

To cite this article: Xinxin He *et al* 2024 *Int. J. Extrem. Manuf.* **6** 032007

OPEN ACCESS
IOP Publishing | IMMT
International Journal of Extreme Manufacturing
Int. J. Extrem. Manuf. 6 (2024) 032007 (33pp)
https://doi.org/10.1088/2631-7990/ad3316

Topical Review

Preparation of single atom catalysts for high sensitive gas sensing

Xinxin He[1,6], **Ping Guo**[1,6], **Xuyang An**[1], **Yuyang Li**[1], **Jiatai Chen**[1], **Xingyu Zhang**[1], **Lifeng Wang**[2], **Mingjin Dai**[3], **Chaoliang Tan**[4] **and Jia Zhang**[1,5,*]

[1] Key Laboratory of Microsystems and Microstructure Manufacturing, Ministry of Education, Harbin Institute of Technology, Harbin 150080, People's Republic of China
[2] Institute for Frontier Materials, Deakin University, Waurn Ponds Campus, Locked Bag 20000, Victoria 3220, Australia
[3] School of Electrical and Electronic Engineering, Nanyang Technological University, Singapore 639798, Singapore
[4] Department of Electrical and Electronic Engineering, The University of Hong Kong, Pokfulam Road, Hong Kong Special Administrative Region of China 999077, People's Republic of China
[5] Chongqing Research Institute, Harbin Institute of Technology, Chongqing 401120, People's Republic of China

E-mail: zhangjia@hit.edu.cn

Received 7 October 2023, revised 21 November 2023
Accepted for publication 12 March 2024
Published 28 March 2024

Abstract

Single atom catalysts (SACs) have garnered significant attention in the field of catalysis over the past decade due to their exceptional atom utilization efficiency and distinct physical and chemical properties. For the semiconductor-based electrical gas sensor, the core is the catalysis process of target gas molecules on the sensitive materials. In this context, the SACs offer great potential for highly sensitive and selective gas sensing, however, only some of the bubbles come to the surface. To facilitate practical applications, we present a comprehensive review of the preparation strategies for SACs, with a focus on overcoming the challenges of aggregation and low loading. Extensive research efforts have been devoted to investigating the gas sensing mechanism, exploring sensitive materials, optimizing device structures, and refining signal post-processing techniques. Finally, the challenges and future perspectives on the SACs based gas sensing are presented.

Keywords: single atom catalysts, preparation, sensing mechanism, gas sensing

---

[6] These authors contributed equally to this work.
[*] Author to whom any correspondence should be addressed.

1. Introduction

Gas sensors have been widely used in the field of respiratory disease diagnosis [1], environmental monitoring [2], indoor air quality testing [3] and food safety [4]. More recently, there has been an increasing need for gas composition detection in extreme environments, such as the Earth's three poles [5], the deep sea [6], and extraterrestrial bodies [7, 8] (e.g. the Moon, the Mars). These demanding environments impose stringent technical requirements on the sensors employed, necessitating further enhancement of their performance. While some gas sensors can presently detect trace-level gases, many still encounter challenges such as low sensitivity, slow response and recovery times, baseline drift, and high operating temperatures [9–13]. To address these challenges, extensive research efforts have been conducted, encompassing investigations into gas sensing mechanisms, sensitive materials, device structures, and signal post-processing techniques.

After more than half a century of research efforts, various quantified gas sensors have been developed alongside the qualitative colorimetric gas sensor [14]. These include sensors based on quartz crystal microbalance [15–19], surface acoustic wave [20–23], semiconductor [24–27], electrochemical and solid electrolyte [28–30] technologies. Among them, semiconductor-based electrical sensors have garnered significant attention due to their high sensitivity, simple manufacturing process, low cost, and compact size. The sensing material plays a crucial role in semiconductor gas sensors as it greatly influences the sensor's performance in terms of sensitivity, selectivity, and response time. Several types of sensing materials have been developed, including metal oxide semiconductors [31–33], carbon-based materials [34–37], conductive polymers [38–41], and emerging two-dimensional (2D) materials [42–44]. In general, the sensing materials should effectively capture target gas molecules and convert gas interactions into detectable signals. Therefore, extensive efforts have been made to optimize the properties of sensing materials, including morphology and crystal structure modulation [45–51], noble metals modification [52–54], heterojunctions construction [55–59], and vacancies insertion [60–63]. Among these approaches, the modification of traditional semiconductor materials with single-atom metals has demonstrated not only high sensitivity and selectivity of target gases but also outstanding utilization rates of noble metals and low synthesis costs [64, 65]. This bears a resemblance to the utilization of metallic single-atom catalysts (SACs) in current catalysis applications [65].

SACs were initially designed and applied in the field of multiphase catalysis [66, 67], exhibiting superior performance compared to their nanoscale counterparts. This can be attributed to their efficient utilization of active sites on metal atoms and the reduction of activation energy in chemical reactions [68–73]. Similarly, gas sensing can be viewed as a multiphase surface catalytic process involving interactions between gas molecules and SACs [74]. Therefore, SACs with well-defined surface properties hold significant potential as sensing materials for target gas detection [75]. Typically, SACs are prepared on supporting material, forming an integrated system for gas sensing. In this context, the supporting material is referred as the 'support', while the combined SACs and support function as sensitive materials for gas sensing. SACs can provide higher sensitivity to specific gas reaction processes and effectively reduce sensor operating temperatures due to their maximum atom utilization efficiency. What's more, the highly homogeneous size and shape of SACs can minimize side reactions and significantly enhance selectivity for specific gas response processes. The application of SACs in gas sensing is expected to enable precise detection of trace level gases [76, 77]. Preliminary studies have demonstrated that single atoms (SAs) of noble metals (e.g. Pt, Au, Ag) loaded onto semiconductor materials (e.g. WO_3) can serve as chemical and electrical sensitizers to enhance gas sensing performance [65, 78, 79]. SACs act as active sites, promoting the adsorption and activation of target molecules [80], as well as the chemisorption of oxygen on the sensing material surface through spillover effects [81]. Moreover, the intrinsic catalytic ability of SACs facilitates the reaction between the sensing material and target gas molecules [82]. Meanwhile, the modification of single atoms can also enhance the electron transport capability of the material by establishing efficient charge transfer channels and Schottky barriers [79, 83]. Therefore, an increasing number of SACs have been employed in gas sensing, showcasing their potential in boosting sensor sensitivity, reducing response and recovery time, and improving the utilization efficiency of precious noble metals [84–86]. Despite these unique advantages, practical applications of SACs for the detection of various gases are still relatively limited. Several challenging issues need to be addressed, including the unclear gas-sensitizing mechanism, the mass-scale preparation of authentic SACs, and the design of specific SACs tailored for target gases.

The recent advancements in the utilization of SACs for gas sensors have been extensively reviewed [64, 65]. Lei *et al* systematically elucidated the evolving landscape of SACs in gas sensing, encompassing SAC synthesis methods, the gas-sensing mechanism of SACs, and the application of distinct metal SACs in gas sensing [64]. The reported attractive sensing performances underscore the pronounced potential of SAC as a superior gas sensing material. Complementarily, Chu *et al* offered a comprehensive summary of SAC applications in gas sensors categorized by the various support materials onto which metal atoms are loaded [65]. However, there remains a notable gap in summarizing diverse target gases and a perspective that would enable readers to efficiently comprehend advancements in sensors tailored for specific gases. Concurrently, this paper provides a comprehensive and systematic exploration of the mechanism through which single atoms enhance sensor performance.

Within this review, we present a systematic overview of the progress made in SACs-based gas sensors (see figure 1). Commencing with an overview of the structural diagrams of the electrical-based gas sensors, this study proceeds to a detailed examination of the preparation methods employed for SACs. Following, the detection principles of SACs-modified gas sensing materials are discussed from two aspects. Firstly, an exploration of the interaction dynamics between SACs and target gases is presented. Secondly, attention is directed

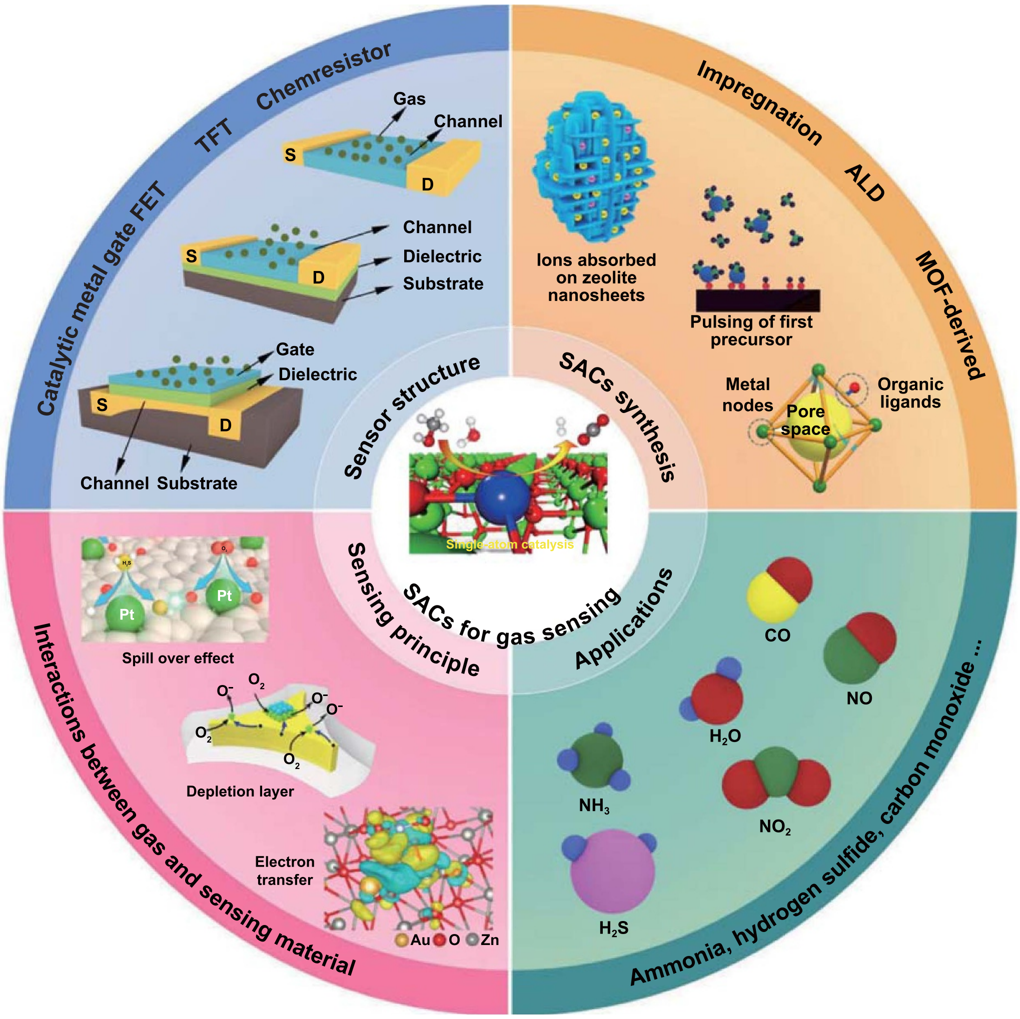

Figure 1. The preparation of SACs and their application in the semiconductor-based gas sensors. Reprinted from [79], © 2019 Elsevier B.V. All rights reserved. Reprinted with permission from [87]. Copyright (2021) American Chemical Society. Reprinted from [88], © 2018 Elsevier Inc. Reprinted with permission from [89].Copyright (2022) American Chemical Society. Reprinted from [90], © 2020 Elsevier Inc. Reprinted with permission from [91]. Copyright (2016) American Chemical Society. Reprinted with permission from [92]. Copyright (2021) American Chemical Society.

towards the interaction mechanisms between SACs and their respective supports. Finally, a comprehensive summation of the applications of SACs in the detection of diverse gases is provided, accentuating the superior performance of SACs-modified sensing materials in comparison to traditional counterparts (refer to figure 1). The paper culminates by proposing a perspective on the utilization of SACs in the realm of gas sensing.

2. Structure and principle of semiconductor gas sensors

Semiconductor-based electrical gas sensors have garnered extensive attention for their notable attributes of high sensitivity and micro/nano-scaled dimensions [26, 78, 93–97]. The typical device structures are elucidated in figure 2, encompassing various configurations such as chemiresistors [98] (figure 2(a)), thin film transistor (TFT) sensors [98] (figure 2(b)), catalytic metal gate field-effect transistor (FET) sensors [26] (figure 2(c)), and suspend gate FET [26] (figure 2(d)).

For the chemiresistors, the resistance will change while the sensitive material is exposed to the target gases [102, 103]. Figure 2(a) schematically illustrates the structure of chemiresistors. To date, the most commonly used sensitive materials are still metal oxide semiconductors and their composites [94, 104–106]. In the air, the oxygen molecules always adsorb on the oxygen defect sites of the sensitive material and extract free electrons from its conduction band, forming negative oxygen species (e.g. O_2^-, O^- and O^{2-}) [79, 107]. This process results in a reduction or even depletion of free electrons in the sensitive material. Therefore an increased resistance as well as a higher potential barrier appears at this point, as presented in figure 2(e) [99]. When exposed to the reducing gases (e.g. NO, CO, H_2O_2), the adsorbed oxygen species will react with them to produce NO_2, CO_2, and H_2O. The previously extracted electrons will rejoin the conduction band of the sensitive material,

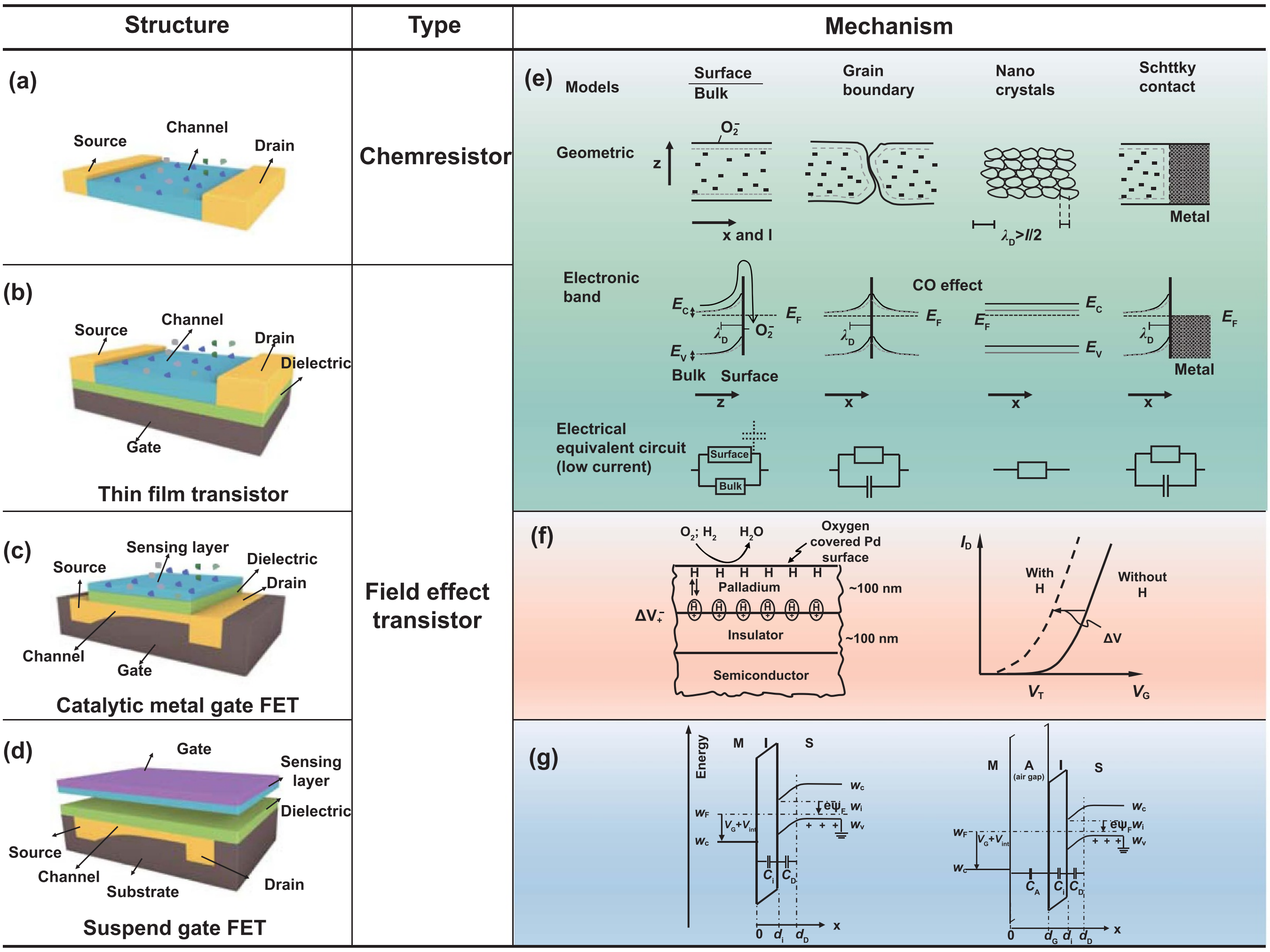

Figure 2. The structure and sensing principle of semiconductor-based gas sensor. The structural scheme of (a) chemiresistor, (b) thin film transistor, (c) sensitive-gate field-effect transistor, and (d) suspended gate FET. (e) Different conduction mechanisms and changes upon O_2 and CO exposure to the sensitive material in overview. The survey shows geometries, electronic band pictures and equivalent circuits, where EC denotes the minimum of the conduction band, EV denotes the maximum of the valence band, EF denotes the Fermi level, and λD denotes the Debye length. Reproduced from [99], with permission from Springer Nature. (f) 'Classical' schematic drawing illustrates the hydrogen sensitive field-effect devices with catalytic metal (Pd) gates, where hydrogen atoms adsorbed at the metal–oxide interface causing a shift of the electrical characteristics along the voltage axis. Reprinted from [100], Copyright © 2006 Elsevier B.V. All rights reserved. (g) Energy band diagrams and schematic series capacitances of conventional MIS (left) and suspended gate MIS (right). Reprinted from [101], Copyright © 2001 Elsevier Science B.V. All rights reserved.

resulting in a reduction of the depletion layer, a decrease in the potential barrier, and an increase in conductivity. Usually, the morphology of the metal oxide (e.g. compact, porous) will influence its interaction with target gases. For the compact materials, the gas is in contact with their surface and its conductivity is modeled as a surface/bulk mold (figure 2(e)) [99]. In the case of porous materials, the gas molecules can absorb on their interiors, resulting in a more complex process to change the conductivity of the material. Therefore, the conductivity model may contain surface/bulk, grain boundary and flat bands (figure 2(e)) [99]. Apart from metal oxides, various other materials such as carbon-based materials (e.g. graphene [108, 109], carbon nanotubes [110, 111]), polymers (e.g. PANI [112, 113], PVDF [114]), 2D materials (TMDs [115, 116], h-BN [117]), have also been explored as potential sensitive materials for gas sensors.

For the TFT sensor, where the sensitive material serves as the channel material, the source-drain current (I_D) changes according to following two mechanisms. On the one hand, the target gas will regulate the conductivity of the sensitive material, similar to the progress described above (figure 2(e)). On the other hand, the adsorption of gas molecules regulates the material's work function, subsequently influencing the Schottky barrier between the channel material and the electrode, thereby modulating the channel current [26, 93, 98]. This observation aligns well with the findings of Heller *et al*, who demonstrated that a synergistic interplay between gate regulation by target molecules and modulation of the Schottky barrier imparts excellent sensing properties to carbon nanotube FETs [118].

For the catalytic metal gate FET sensor (figure 2(c)), the I_D is decisively influenced by the electric field generated by the gate voltage. Upon the interaction of target gases with the sensitive material, an external electrical field is generated, which synergistically combines with the pre-existing field, resulting in a modulation of the I_D. The deliberate choice of specific sensitive materials enables the detection of corresponding gases [95, 96]. Usually, palladium (Pd) is a frequently-used material in the highly sensitive detection of hydrogen. The hydrogen bond breaks at the step defects of Pd nanoparticles, resulting in the formation of free radicals. These entities can migrate toward the interface between the gate and the dielectric layer, thereby establishing a dipole layer (left part of figure 2(f)) [100]. The electric field emanating from the established dipole layer is overlaid upon the intrinsic electric field within the device, consequently modifying the effective gate voltage of the FET (right part of figure 2(f)). As a result, depletion layer thickness and Schottky barrier height of the channel will change, influencing the current of device, thereby indicating the concentration of target gases [119]. The sensor based on the catalytic metal gate FET shows superior performance compared with the aforementioned two schemes under the same condition. This can be attributed to the utilization of bottom gate in the sensor's structure. As shown in figure 2(f), the initial state of the FET can be adjusted to the point where the slope of the *I*–*V* curve arrives at its maximum. As a consequence, a subtle perturbation of the electric field, induced by the presence of gas molecules, can evoke a robust response from the device. By using this scheme, Yuan *et al* obtained ultra-sensitive silicon-based sensors for ammonia, hydrogen sulfide, and humidity via using ruthenium, silver, and silicon oxide as sensing materials, respectively [95]. The detection limit was as low as 10 ppb for ammonia and hydrogen sulfide, demonstrating the great potential of gas sensors based on catalytic metal gate FETs [95].

For the suspended gate FET, the structure is schematically illustrated in figure 2(d), where an air gap exists between the suspension gate and the dielectric layer. The target gas flows through the gap and reacts with the sensitive material on the gate, changing the work function of gate and thus the channel current of the device. The threshold voltage for the conventional metal oxide semiconductor FET (left part of figure 2(g)) can be calculated by the following formula,

$$V_T = 2\varphi_B + \Phi_{ms} - \frac{1}{Cd}\int_0^d x\rho(x)\,dx + \frac{Q_D}{C} \tag{1}$$

where, φ_B represents the potential difference between the intrinsic and Fermi energy levels of the semiconductor, Φ_{ms} represents the difference of work function between the gate and the semiconductor. The parameters of C, d, ρ and Q_D denote the capacitance between the metal gate and the semiconductor channel, the distance, the charge density in the insulator and the depletion charge density of the semiconductor, respectively. The V_T of suspended gate FET can be calculated according to formula (1) by taking the capacitance of air gap into consideration (right part of figure 2(g)). The value of V_T will change according to Φ_{ms} (formula (1)) when the sensor is exposed to target gas, leading to a parallel shift in I_D–V_G curve (figure 2(f)). As a result, the change in current can indicate the change in gas concentration. However, the fabrication of the air gap presents significant challenges, rendering this sensor structure less prevalent in contemporary usage.

3. Preparation of single atom catalysts

The preparation of SACs for chemical catalysis and sensing is actually to immobilize single or few atoms on the support materials. Nevertheless, the specific surface area experiences a notable increase as the metal particle size diminishes to the single atom level, consequently leading to a significant elevation in the surface energy of SACs. As a result, the thermal and chemical stability of SACs is compromised, rendering them susceptible to the facile migration and aggregation of individual atoms [120, 121]. Up to now, it is still a challenge to prepare SACs with high loading, high dispersion, and strong metal-support interactions. To overcome this challenge, various strategies have been developed to prepare SACs, including impregnation [122–124], co-precipitation [125, 126], one-pot pyrolysis [127–129], atomic layer deposition (ALD) [130–132], sacrificial template [133, 134], and metal organic framework (MOF) derived approach [135–137], among others. The proposed strategies have their own advantages, disadvantages and specific applicability. For instance, wet chemistry methods (such as wet impregnation and co-precipitation) are the most practical and cost-effective approaches for preparing SACs, particularly for large-scale production. Pyrolysis is increasingly becoming the mainstream method for synthesizing SACs with high metal loadings. ALD allows for the uniform deposition of SACs on supports with high surface area. In this section, the strategies of preparing SACs will be discussed in detail to provide a theoretical basis for the subsequent development of more effective SACs for gas sensing.

3.1. Impregnation

The impregnation is a classic method for preparing SACs. As depicted in figure 3(a), the support is initially immersed in a solution containing metal ions, facilitating the atomic-level dispersion of metal ions on its surface through adsorption and diffusion. Subsequently, the support undergoes a sequential series of washing, drying, and annealing processes, culminating in the deposition of metal ions onto the support in a limited quantity [138]. For example, Wang *et al r*eported the anchoring of Rhodium-Ruthenium (Rh-Ru) atoms on the surface of self-column-supported MFI zeolites (silicalite-1 and ZSM-5) (figure 3(a)), which had a large specific surface area and abundant Si-OH groups, thereby enhancing the hydrophilicity and transport efficiency massively. The Rh–Ru atoms are confined within the five-membered ring of MFI, highlighting the zeolite nanosheet's efficacy as an exceptional support for immobilizing ultra-small metal species [87]. To enhance the loading of SACs further, modifying the substrate to provide abundant anchoring points proves to be an efficient approach. Zhang *et al* reported that the $[PtCl_6]^{2-}$ ions can be trapped by hierarchical N-doped carbon nanocages

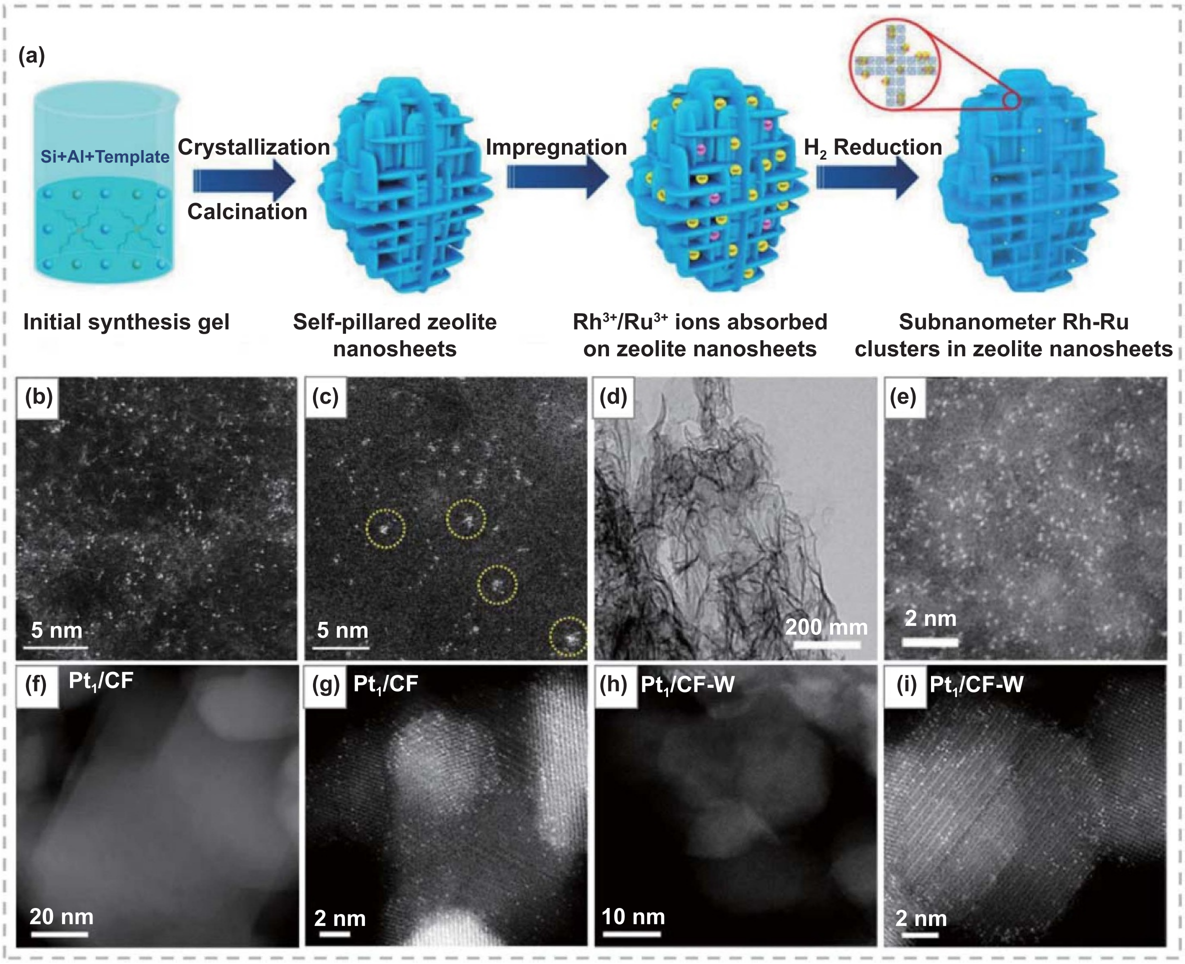

Figure 3. Preparation of SACs via impregnation method. (a) Schematic illustration of the synthetic procedure of sub-nanometer Rh–Ru clusters in self-pillared MFI nanosheets. Reprinted with permission from [87]. Copyright (2021) American Chemical Society. (b) and (c) HAADF-STEM images of Pt SA on the hierarchical N-doped carbon nanocages (Pt(SA)/hNCNC) and Pt SA on the hierarchical carbon nanocages (Pt(SA)/hCNC), respectively. The yellow circles in (c) mark the slight aggregation of Pt atoms. Reproduced from [125]. CC BY 4.0. (d) Low-magnification TEM image of Co(SA)N4/NG. (e) HAADF-STEM image of the Co(SA)N4/NG with Co atom identified by the bright points. Reprinted from [126], © 2018 Elsevier Ltd. All rights reserved. HAADF-STEM images of Pt(SA)/CoFe2O4 and Pt(SA)/CF before (f) and (g) and after (h) and (i) the water treatment, respectively. Reproduced from [142]. CC BY 4.0.

(hNCNCs) and anchored by the N atoms on the micropore edges [125]. Hence, the N-doped nanocages were more effective in preventing the aggregation of Pt atoms (figure 3(b)) compared to pure nanocages (figure 3(c)). The synergistic effect of microporous trapping and nitrogen anchoring proves highly advantageous for immobilizing $[PtCl_6]^{2-}$ anions and the resultant Pt atoms. As a result, the Pt SACs obtained exhibit remarkable stability and catalytic activity. Moreover, this method can be extended to the preparation of SACs using other noble metals, including Pd, Au, and Ir [139–141]. In addition to the trap structure and doped element, the presence of a surfactant can enhance the interaction between the metal and the carrier, thereby promoting the formation of SACs. During the synthesis of single-atom cobalt (Co) electrocatalyst, a water-soluble surfactant (F127) composed of polyoxyethylene- polyoxypropylene-polyoxyethylene (PEO-PEO-PEO) was introduced. This resulted in the dispersion of CoN_4 moieties on N-doped graphitic nanosheets, denoted as $Co(SA)N_4/NG$. TEM images (figures 3(d) and (e)) reveal the uniform distribution of Co SA on a graphene-like nanosheet, without the presence of any Co NPs. The excellent dispersion of Co atoms can be attributed to the strong attraction between the negatively charged F127 and positively charged Co ions [126]. More recently, Yang *et al* presented a modified impregnation method to precisely modulate the strong covalent metal-support interaction of $Pt(SA)/CoFe_2O_4$ by adjusting the neighboring environments of Pt SA through a simple water treatment [142]. High-angle annular dark-field scanning transmission electron microscopy (HAADF-STEM) images (figures 3(f)–(i)) confirm that Pt specie solely exists as the single atoms, while the water treatment does not affect the dispersion of Pt atoms.

In summary, the impregnation method is versatile and can be applied to other materials with metal-support interactions. It is particularly well-suited for immobilizing single atoms on open supports, especially on individually isolated nanostructures [143]. Specifically, the metal precursor is of great importance for the preparation of SACs. While offering the advantage of practical simplicity and low cost, this method presents at least two drawbacks. Firstly, it tends to result in low metal loading, largely contingent upon the precursor-support interaction [144]. The other is the non-uniform dispersion of SACs on the support, which is caused by a few of bondings between the metal precursor and the support. The single atoms can aggregate together during the actual catalytic process, which significantly reduces the activity and selectivity of the SACs [144]. In the future, the key focus of research on the impregnation method will be on increasing metal loading while concurrently preventing the aggregation of atoms. The shortcomings of the traditional impregnation method can be remedied by adjusting the metal-support interaction or by using it in combination with other techniques such as surface engineering. More importantly, optimizing the preparation parameters is practical for tuning the size, accessibility and distribution of the active metal particles as well [145].

3.2. Co-precipitation

Co-precipitation is another widely used typical method for preparing SACs. Unlike the impregnation method, this method usually obtains polymetallic atom co-doped materials with a uniform distribution of active species [120]. Specifically, SACs are obtained by adding a precipitant to a solution containing two or more cations, followed by drying or calcination of the resulting deposit. Thus, it is considered to be an effective method for the preparation of homogeneously dispersed composite oxides containing two or more metal elements. The method has the advantages of a simple process, cost-effectiveness and a short synthesis cycle, resulting in the explosive growth of SAC synthesis.

A variety of noble metal single atoms, such as Au [146], Ag [147], Pt [148], Ir [69], have been synthesized by co-precipitation method, which demonstrates its excellent activity. Fan *et al* presented a novel silver-manganese nanocatalyst, which was synthesized by the silver (Ag) atoms entering the lattice tunneling of Holland-type manganese oxide (HMO) under H_2 reduction at 200 °C (figure 4(a)). The Ag atoms are initially loaded mostly on the HMO surface and only a few enter the lattice tunnels (the third part of figure 4(a)) [147]. The following H_2 reduction facilitates the process of Ag atoms entering the lattice tunnels further, thereby promoting the formation of a sequence of Ag atoms (the fourth part of figure 4(a)). Li *et al* reported a highly efficient Ru(SA)/FeO_x catalyst with various Ru SA loadings obtained by the co-precipitation. For low loading of 0.18 wt%, Ru species exists as single atoms uniformly distributed on the FeO_x surface (marked by yellow circles in figures 4(b) and (c)), in which the Ru SA occupies the positions of the Fe atoms and can be stabilized as Ru–O–Fe molecules. As the loading increases, some of Ru atoms can aggregate into nanoclusters and nanoparticles (NPs). Figures 4(d) and (e) show the Ru nanoclusters and nanoparticles (marked with squares) when the Ru loading increases to 2.56%wt and 2.00%wt, respectively [149].

Besides the noble metal SACs, the non-noble metal SACs can also be prepared via co-precipitation. For example, nickel (Ni) single atoms (SA) dispersed in the MgO lattice (Ni(SA)/MgO) catalysts were prepared for CO_2 activation, in which the $Ni_xMg_{1-x}(OH)_2$ precursor was first synthesized by co-precipitation method, and then calcined in a rotating furnace at 600 °C. Figures 4(f) and (g) exhibit the atomically dispersion of Ni SA in the MgO lattice, in which the Ni atoms possess isolated features with high loading. As a result, the Ni SACs exhibit premium activity toward CO_2 activation in the reverse-water gas-shift reaction [150]. Zhu *et al* prepared Cu SA on the SiO_2 (Cu(SA)/ SiO_2) using urea hydrolysis assistant deposition precipitation. To demonstrate the atomically doping of Cu on SiO_2, they conducted electron beam irradiation on the fabricated material. There is no aggregation of Cu atoms until irradiated for 960 s (figures 4(h) and (i)), when Cu nanoparticles start to emerge. The high copper (Cu) loading (15 wt%) and excellent dispersion of Cu surface area (Cu SA) (83%) in the catalyst are attributed to the synthesis method employed. The utilization of urea hydrolysis facilitates the formation of a robust chemical bond (Cu–O–Si) instead of relying on electrostatic interaction. In addition to the aforementioned non-noble metal, other metal SAs, including manganese (Mn), iron (Fe), cobalt (Co), nickel (Ni), and zinc (Zn), can also be prepared through co-precipitation [151].

In summary, the co-precipitation method exhibits similar advantages to impregnation, making it a commonly employed technique for the preparation of SACs [69, 120]. However, there are still several challenges that need to be addressed in future research. The loading of SACs remains relatively low, and their distribution is not sufficiently uniform. Additionally, SACs tend to be buried in the interior of the supports or anchored to the interfaces of the supports, significantly impacting the catalytic efficiency. To overcome these limitations, strict control of experimental parameters, including temperature, pH, precursor droplet speed, droplet size, stirring intensity, and synthesis time, is necessary. Furthermore, the utilization efficiency of SACs can be enhanced by combining co-precipitation with sponge materials.

3.3. One-pot pyrolysis

The one-pot pyrolysis method serves as an efficient approach for executing multistage reactions using simple feedstock without intermediate separations. In this method, metal complexes typically function as monoatomic precursors, while polymers serve as support precursors [127–129]. In essence, the high-temperature calcination breaks metal–metal bonds or metal-O-metal bonds, leading to the dissociation of metal species and the formation of stable SACs through reinforced interactions between metal atoms and the support [69]. One-pot pyrolysis is commonly employed for synthesizing target products from readily available raw materials, thereby reducing the complexity of precursors and post-processing. This method offers the advantages of a straightforward process and cost-effective raw materials. The synthesized SACs exhibit remarkable thermal stability and catalytic properties.

To achieve the atomic dispersion of metal atoms, Wei *et al* synthesized cobalt SACs on nitrogen-doped carbon supports

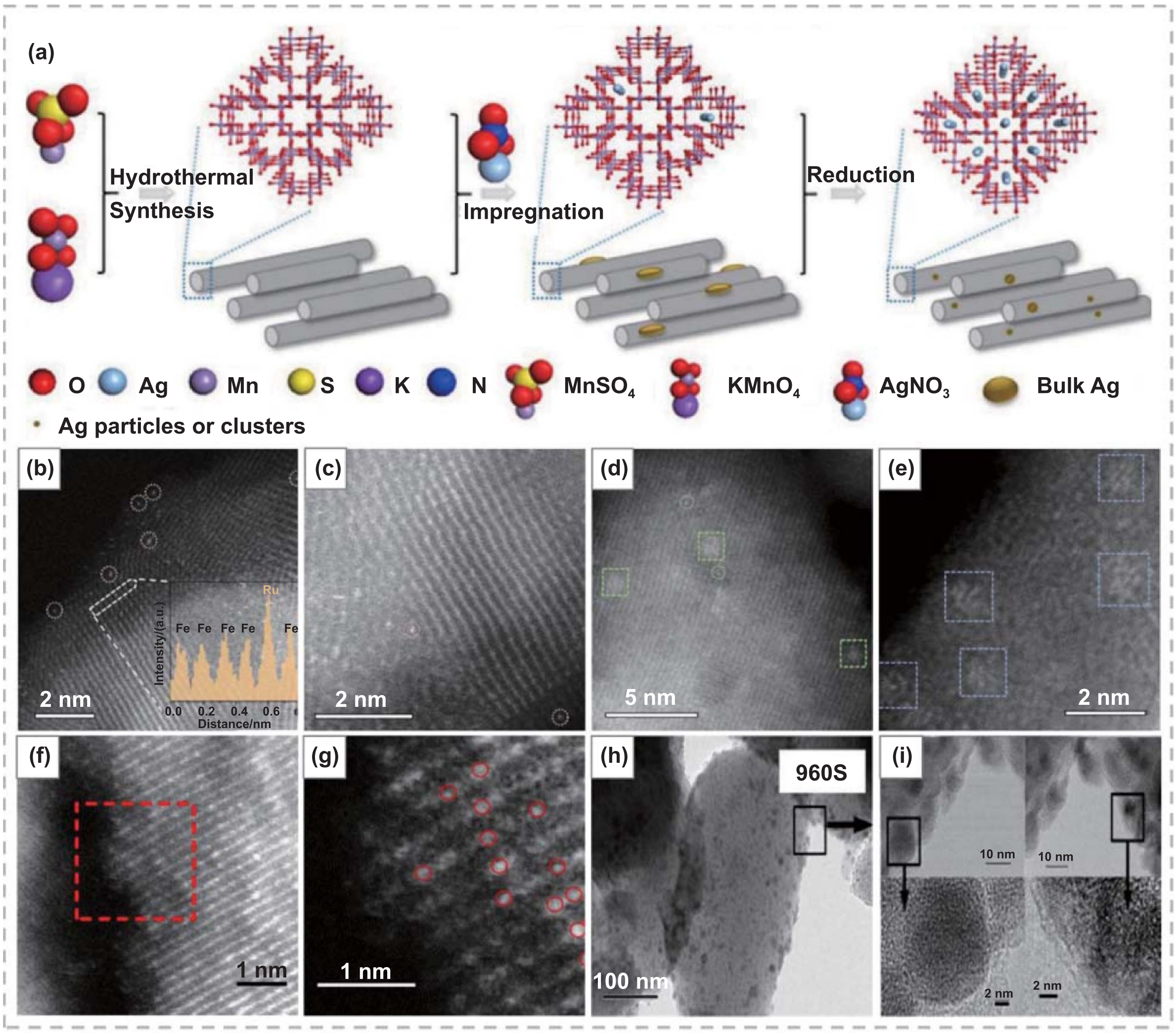

Figure 4. Preparation of SACs via co-precipitation method. (a) Scheme of formation of Ag SACs in the HMO. Reprinted from [147], © 2018 Elsevier B.V. All rights reserved. (b) and (c) Aberration-corrected high-angle annual dark-field scanning transmission electron microscopy (AC-HAADF-STEM) images of Ru(SA)/FeO_x (0.18 wt % Ru loading) with the Ru single atoms marked with yellow circles. (d) and (e) AC-HAADF-STEM images of Ru(SA)/FeO_x with Ru loading of 2.56 wt % and 2.00 wt %, respectively. Reprinted from [149], © 2022 Elsevier B.V. All rights reserved. (f) HAADF-STEM image of Ni(SA)/MgO with Ni loading of 10 atom% before catalytic testing. (g) Enlarged image marked with red box in (f). Reproduced from [150]. CC BY 4.0. (h) and (i) HRTEM images of reduced Cu(SA)/SiO_2 during electron beam irradiation. Reprinted from [151], © 2017 Elsevier Inc. All rights reserved.

(Co(SA)/N-C). In their approach, they utilized cost-effective urea and glucose as nitrogen and carbon precursors, and Co^{2+}-SCN^{-} coordination compounds (Co^{2+}-SCN^{-}) as metal precursors [152]. The decomposition temperature of Co^{2+}-SCN^{-} is lower than the deposition temperature of carbon layers, effectively inhibiting the formation of Co-C structure and instead leading to the initial formation of Co-rich particles at 600 °C. Subsequently, Co atoms are able to escape from the cobalt-rich particles and traverse the discontinuous carbon layer, ultimately forming Co(SA)/N-C catalysts through coordination with nitrogen atoms. Similarly, Qi *et al* employed a similar strategy to achieve a sustainable synthesis of nitrogen-coordinated Co SACs (Co(SA)/N–C) by utilizing lignin as the carbon support for capturing atom-sized metal particles [153]. HAADF-STEM images and x-ray absorption spectroscopy analyses reveal that the isolated Co atoms exhibit sizes smaller than 2 Å. Notably, the method also enables the attainment of ultrahigh metal loading. For instance, Zhao *et al* successfully synthesized Ni SA stabilized on nitrogen-doped carbon nanotube structures (Ni(SA)/N-CNT) with a nickel atom loading up to 20.3 wt% [128]. The yield is intricately linked to the precursor ratio and annealing temperature. X-ray absorption near edge structure simulations and x-ray absorption fine structure (EXAFS) fitting provide a rational explanation for the formation mechanism of Ni(SA)/N-CNT and elucidate the reasons behind the achieved high metal loading. The Ni SA are effectively stabilized by four N-coordinated shells ($Ni–N_4$) surrounded by two carbon-shells, preventing undesired agglomeration.

In summary, the one-pot pyrolysis method provides a pathway for the formation of thermodynamically stable metal-deficient bonds, enabling the achievement of high loading

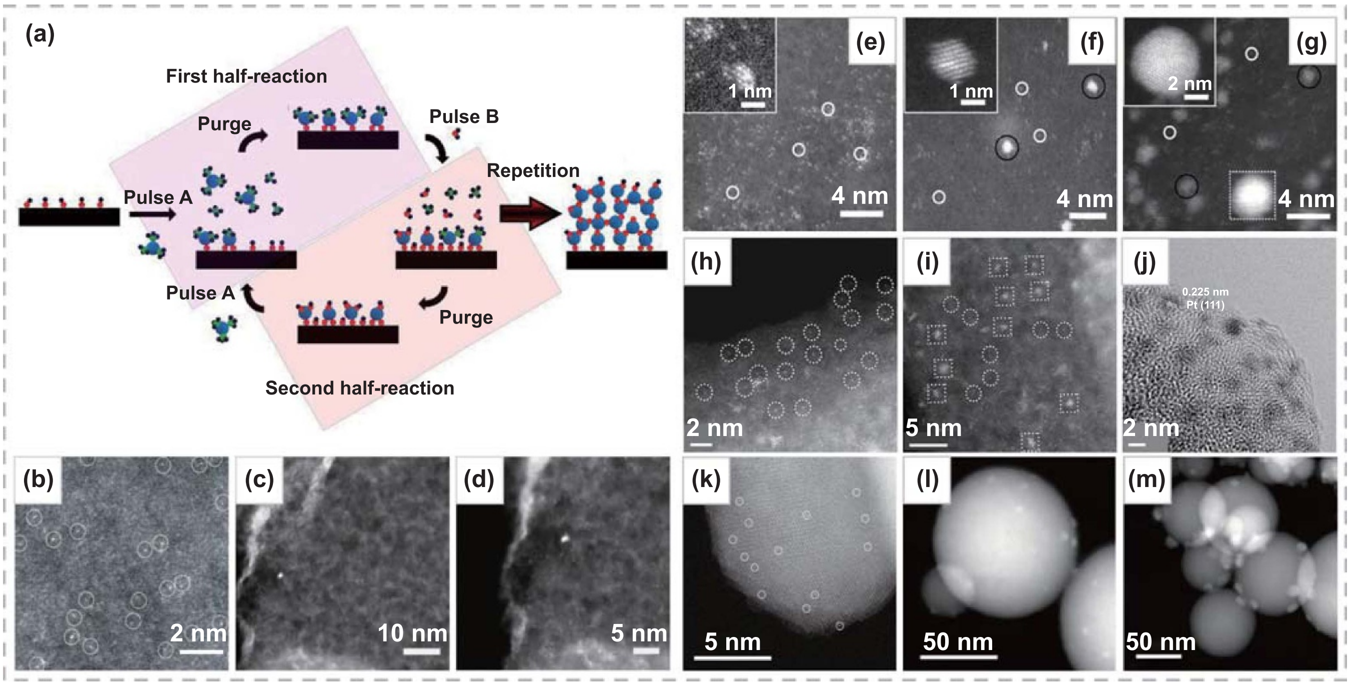

Figure 5. Preparation of SACs via ALD process. (a) Schematic illustration of a general ALD process. Reprinted with permission from [92]. Copyright (2021) American Chemical Society. (b) HAADF-STEM images of Pd(SA)/GNS at high magnifications. The Pd SA is highlighted by the white circles. Reprinted with permission from [132]. Copyright (2015) American Chemical Society. (c) and (d) ADF-STEM images of Pt(SA)/NGNS samples with 50 ALD cycles. Reproduced from [162]. CC BY 4.0. (e)–(g) The Pt(SA)/GNS fabricated from 50, 100, and 150 ALD cycles, respectively. Inset in each figure shows the corresponding enlarged view of Pt SA on the graphene nanosheet. Reproduced from [163], with permission from Springer Nature. © 2013, The Author(s). (h) HADDF-STEM images for Pt(SA)/ZIF-NC prepared with exposure in $MeCpPtMe_3$ precursor for 30 s (Pt SA marked in the circle). (i) HADDF-STEM images of Pt(SA)/ZIF-NC prepared with exposure in $MeCpPtMe_3$ precursor for 1 min (Pt subclusters marked in the square and Pt SA marked in the circle). (j) HADDF-STEM images Pt(NP)/ZIF-NC with exposure in $MeCpPtMe_3$ precursor for 5 min. [164] John Wiley & Sons. © 2020 Wiley-VCH GmbH. (k) STEM images of $Cu(SA)/Al_2O_3$ obtained from one ALD cycle performed at 250 °C. (l) and (m) STEM images of $Cu(NP)/Al_2O_3$ obtained from one and five ALD cycles performed at 300 °C, respectively. Reprinted with permission from [165]. Copyright (2020) American Chemical Society.

and highly active SACs. However, the elevated reaction temperatures associated with this method not only result in significant energy consumption but also contribute to the pronounced tendency of SAC agglomeration. Therefore, it becomes imperative to carefully choose a suitable support, such as MOFs, which can facilitate the dispersion of SACs on a non-homogeneous support and reduce binding energy. This, in turn, effectively inhibits the agglomeration of individual metal atoms. Furthermore, the combination of one-pot pyrolysis with other strategies holds promise for the fabrication of highly active SACs.

3.4. Atomic layer deposition

ALD is a cyclic process that relies on the self-limiting surface reaction between gas-phase precursors and solid surfaces [92, 154]. This technique offers the capability to uniformly distribute nanoparticles on suitable supports, ranging in size from nanometers to single atoms [155–158]. Additionally, ALD exhibits the ability to penetrate high surface area porous supports, making it well-suited for the synthesis of gas sensing materials [159]. Typically, the preparation of SACs via the ALD technique involves four steps (figure 5(a)) [92, 130–132]. Firstly, the support is exposed to the vapor of the first precursor, which chemically reacts with or adsorbs onto the support surface. Secondly, inert gas purging and evacuation are employed to remove excessive precursor molecules and by-products from the support surface. Thirdly, the support is exposed to the vapor of the second precursor, which removes the remaining ligands from the first precursor and generates active sites for the subsequent cycle. Finally, the same setup as in the second step is used to remove excessive precursor molecules and by-products [92, 131, 160]. The shape, size and quality of the deposited material can be controlled by manipulating the parameters during the ALD cycle [161]. Recently, ALD has been employed to fabricate SACs with enhanced loading capacity and thermal stability through the precise control of parameters and modification of support materials.

The support material plays a critical role in providing anchoring sites for the metal atoms, thus influencing the stability of SACs. Yan *et al* achieved controllable introduction of oxygen functional groups onto graphene through a series of oxidation and partial reduction processes. This resulted in a graphene support with predominantly phenolic oxygen groups as anchoring sites for Pt SA [132]. Additionally, they successfully synthesized atomically dispersed Pd SACs on the graphene nanosheets (Pd(SA)/GNS) (figure 5(b)), which exhibited an excellent resistance to deactivation. Furthermore, heteroatom doping on the graphene lattice can also serve as anchor sites. As shown in figures 5(c) and (d), Pt atoms were deposited on nitrogen-doped graphene nanosheets (Pt(SA)/NGNS). First-principles calculations demonstrated the effectiveness of nitrogen doping in stabilizing Pt atoms, with a stronger interaction between Pt and nitrogen atoms (5.3 Ev) compared to that between Pt and carbon atoms (3.4 Ev) [162].

Besides the structure of the support, the reaction parameters employed during the ALD process also have a great influence on the morphology and size of the resulting material. Sun *et al* conducted a comparative analysis of the morphology of Pt atoms deposited on graphene nanosheets (Pt(SA)/GNS) obtained through varying ALD cycles. Figure 5(e) illustrates the morphology of Pt SACs obtained after 50 cycles, revealing predominantly isolated Pt atoms with occasional clusters and nanoparticles. However, with an increase in the number of cycles to 100 (figure 5(f)) and 150 (figure 5(g)), the initially monoatomic Pt species aggregated into clusters and nanoparticles [163]. The aggregation of single atoms may result from their weak interaction with the support material, and on the other hand, the extremely high surface energy of isolated metal atoms [120]. Moreover, the duration of exposure to the Pt precursor can also have a great influence on morphology of SACs. Figure 5(h) shows the uniform distribution of Pt SA on MOF-derived nanocarbon (Pt(SA)/ZIF-NC) achieved through a precursor exposure time of 30 s, with a Pt loading of 0.8 wt%. However, as the precursor exposure time increases to 1 min and 5 min, the Pt entities evolve into subclusters (Pt(SC)/ZIF-NC) measuring 0.85 nm in diameter, with a Pt loading of 1.5 wt% (figure 5(i)), and subsequently into nanoparticles (Pt(NP)/ZIF-NC) measuring 2 nm in diameter, with a Pt loading of 10.5 wt% (figure 5(j)) [164]. Shi *et al* systematically adjusted the size of Cu species on alumina supports (Cu(SA)/Al_2O_3) by meticulously controlling the ALD reaction temperature. At a reaction temperature of 250 °C, the Cu species were observed to be atomically dispersed on the support, as depicted in figure 5(k), with a loading of 0.5 wt%. However, with an increase in the reaction temperature to 300 °C, the Cu species exhibited growth to (3.4 ± 1.1) nm, accompanied by a loading of 0.8 wt%, as illustrated in figure 5(l). Consistent with the observations made by Sun *et al* [163], Shi *et al* note that an augmentation in the number of cycles led to an enlargement of Cu nanoparticles. Figure 5(m), a STEM image of Cu(NP)/Al_2O_3 obtained after five cycles at 300 °C, revealed an increased Cu particle diameter of (9.3 ± 1.6) nm, contrasting with the 3.4 nm diameter observed after a single cycle [165].

Primarily, the ALD technique provides precise control over the morphology of SACs by manipulating both the parameters of the reaction cycle and the characteristics of the support material. Simultaneously, SACs can be consistently and reproducibly produced through a stringent manufacturing process. However, the tendency of newly synthesized single atoms to aggregate with existing ones during the cycling process often leads to the undesired formation of clusters and nanoparticles. To enhance the loading capacity of SACs and mitigate aggregation, it becomes imperative to further augment the interaction between metal atoms and supports. For instance, the deliberate choice of supports, coupled with precise control of anchor points by manipulating reaction conditions, represents promising avenues to attain SAC materials characterized by elevated loading capacity and enhanced stability [92].

3.5. MOF-derived SACs

With the merit of low energy consumption and high scalability, the MOF-derived method has emerged as a promising approach for the preparation of SACs. Typically, MOFs are crystalline porous materials with a high specific surface area, assembled through the coordination between metal ions or clusters and organic linkers. The distinctive features of MOFs, including their well-defined structure, robust designability, and intricate network of channels, render them exceptionally suitable as supports for SACs. To date, at least three strategies have been employed for anchoring metal atoms on MOF supports. These strategies encompass the use of functional organic linkers, coordinative unsaturated metal clusters, and the intermediate micropores formed by organic frameworks (figure 6(a)) [88].

Metal clusters possessing unsaturated coordination sites can serve as anchoring sites for target metal atoms by offering unoccupied sites for their accommodation. In this approach, the desired metal atoms presented within the metal ligands of MOFs are reduced through processes such as pyrolysis, resulting in the formation of single atoms loaded onto the support. Yin *et al* successfully synthesized single-atom Co catalyst on nitrogen-doped porous carbon surfaces (Co(SA)/N-C) by subjecting bimetallic Zn/Co organic frameworks to pyrolysis under a nitrogen atmosphere [166]. The schematic diagram presented in figure 6(b) illustrates the formation mechanism of stable single-atom Co catalysts. During the pyrolysis process, the organic linkers of the MOFs transform into N-doped porous carbon support, while the Co species presented in the ligands undergo reduction to form individual Co atoms.

The pre-doped Zn ligand served as an isolator for Co atoms, preventing their aggregation. The Zn ligand evaporates during the pyrolysis process due to its lower evaporation temperature, creating vacancies for N atoms doping. The obtained Co SACs (figure 6(c)) have exhibited excellent chemical and thermal stability during the electrocatalytic process. Jiao *et al* synthesized Fe SA on N-doped porous carbon (Fe(SA)/N-C) with a high loading (1.76 wt%) by pyrolyzing porphyrin MOFs with two kinds of ligands (Fe-TCPP and H_2-TCPP, TCPP is an abbreviation of tetrakis (4carboxyphenyl)porphyrin)) [169]. The Fe(SA)/N-C shows favorable redox activity and stability in both alkaline and acidic environments. Consequently, the MOFs-based hybrid ligand strategy is anticipated to be a versatile method for preparing SACs.

Alternatively, the metal precursors can be accommodated by the pore space of the MOFs, as schematically illustrated in figure 6(d). The zeolitic imidazolate frameworks (ZIF-8), with a cavity diameter of 11.6 Å and a pore diameter of 3.4 Å, can

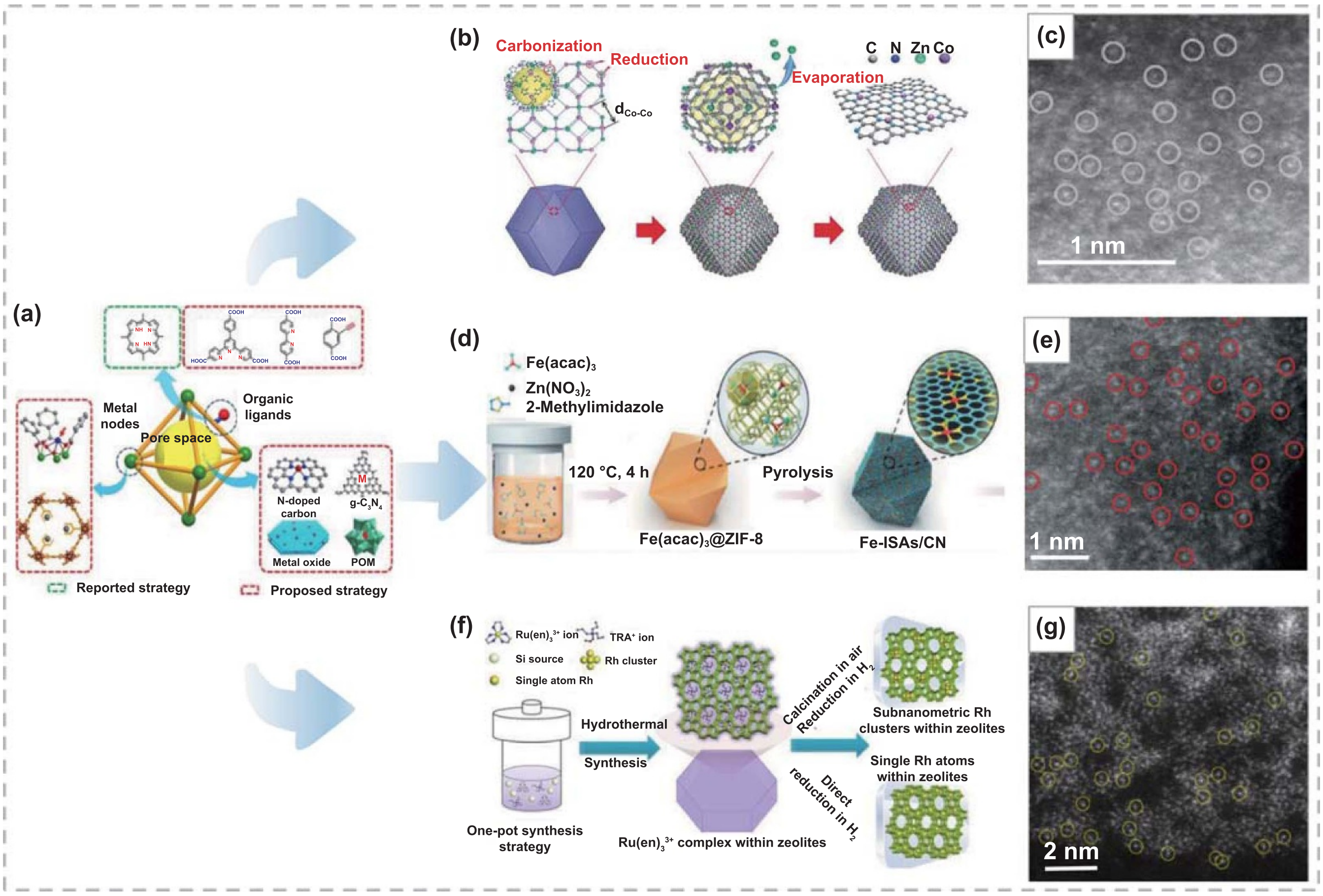

Figure 6. Preparation of MOF-derived SACs. (a) Various strategies to anchor metal SAC by MOF. Reprinted from [88], © 2018 Elsevier Inc. (b) Schematic illustration of anchoring sites provided by metal ligands anchoring target metal atoms. (c) HAADF-STEM image of Co(SA)/N-C, showing that only Co SA is presented in the synthesized material [166]. John Wiley & Sons. © 2016 WILEY-VCH Verlag GmbH & Co. KGaA, Weinheim. (d) Schematic illustration of the MOFs pore space separating metal atoms. (e) The HAADF-STEM image of the Fe(SA)/N-C. The single Fe atoms are highlighted by red circles [167]. John Wiley & Sons. © 2017 Wiley-VCH Verlag GmbH & Co. KGaA, Weinheim. (f) Schematic illustration of the anchoring sites provided by organic linkers [135]. John Wiley & Sons. © 2019 Wiley-VCH Verlag GmbH & Co. KGaA, Weinheim. (g) HAADF-STEM image of Pt(SA)/Ce-MOF. The single Pt atoms are highlighted by yellow circles. Reprinted with permission from [168]. Copyright (2020) American Chemical Society.

act as a molecular cage to immobilize and isolate the metal precursor tris(actylacetonato) Iron(III) (Fe(acac)$_3$) with a molecular diameter of approximately 9.7 Å. The Fe(acac)$_3$/ZIF-8 composite material was subsequently subjected to pyrolysis at 900 °C. During this process, the Fe(acac)$_3$ within the cage underwent reduction due to the carbonization of organic linker, and ZIF-8 was transformed into N-doped porous carbon. As a result, this process produces the isolated Fe SA on N-doped porous carbon (Fe(SA)/N-C) (figure 6(e)). In particular, the iron loading can be increased to 2.16 wt%, resulting in catalytic activity that surpasses that of most non-noble metal ORR catalysts [167]. Liu *et al* employed molybdenum-based Anderson polyoxometalate clusters ($RhMo_6O_{24}^{n-}$ and $Mo_7O_{24}^{m-}$; POMs) to isolate Rh atoms, which were subsequently assembled and grafted onto hierarchically porous Zr(IV)-based MOF (NU1K) to spatially isolate Rh. The orientation restriction of POM in NU1K facilitated the easy accessibility of the prepared Rh SA to target gases. Their work showcased the effectiveness of utilizing the MOF/Anderson POM combination for synthesizing stable, homogeneous, high specific area SACs [170]. In addition to monoatomic catalysts, the method can also be employed to prepare polyatomic catalysts with precise control. For instance, Wu *et al* successfully obtained Ru catalysts (Ru(SA)/N-C and Ru$_3$/N-C) loaded on nitrogen-doped carbon materials using a ZIF-8 isolated precursor strategy [171].

Furthermore, the desired metal atoms can be effectively stabilized through coordination sites provided by functional organic linkers. Essentially, this method involves immobilizing the metal precursor using the MOF's organic linkers, followed by reduction through pyrolysis or other methods to obtain the desired metal single atoms. As an illustration, Sun *et al* embedded Rh precursors into MFI-type silicalite-1 (S-1) and aluminosilicate ZSM-5 zeolites molecular sieves. They obtained Rh SACs through subsequent hydrogen reduction (figure 6(f)) [135]. During this process, the Rh precursor is immobilized by oxygen atoms on the zeolite framework, thereby preventing aggregation during reduction and application. In addition to the coordination sites provided by the MOF itself, it is also feasible to enhance the number of anchoring sites by intentionally introducing defects into the MOFs. Guo *et al* acquired the well-dispersed Pt atoms mediated by cerium-MOF (Pt(SA)/Ce-MOF) through the photoreduction of Pt precursor. This precursor is immobilized at intentionally created defects on Ce-MOF (figure 6(g)). The Pt SAC demonstrates a capability to achieve 100% CO conversion at a working temperature of 150 °C, with a content as low as 0.12 wt% [168]. Analogously, Yin *et al* obtained the well-dispersed single-atom Fe catalysts (Fe(SA)/N-C) dispersed on 2D hierarchical porous N-doped carbon nanosheets. This was achieved through the coordination and steric hindrance between Fe^{3+} and benzidine hydrochloride, preventing aggregation during the pyrolysis process [172].

The MOF-derived method, employing various strategies to stabilize metal atoms, represents a practical approach for synthesizing SACs. However, these strategies are only applicable to specific systems. Furthermore, the loading of SACs remains relatively low, thereby limiting their practical applications. Hence, the development of a simple and scalable method to prepare MOF-derived SACs with high loading remains a significant challenge. It is anticipated that the loading can be enhanced by designing and customizing MOFs to precisely control the coordination environment of single atoms. Additionally, porous polymer materials, such as covalent organic frameworks and hydrogen bonded organic frameworks, hold promise as potential platforms for fabricating SACs due to their analogous structural frameworks with MOF.

3.6. Sacrificial template

The sacrificial template method is a prevalent and effective approach for synthesizing metal oxides at the micro/nanometer scales. It has been introduced in the synthesis of SACs to enhance the loading of single atoms [134, 173, 174]. The utilization of a hard template has the potential to promote the dispersion of the metal, resulting in a catalyst with a higher number of exposed active sites and a greater specific surface area [175]. For instance, Shin *et al* obtained highly dispersed Pt atoms (figures 7(b)–(d)) supported on various supports (SnO_2/ $LaCoO_3$/Pd) with a Pt loading up to 3.94 wt% using the sacrificial template method. In this technique, the nanosheets (NSs) of metals or metal oxides are synthesized by employing graphene or graphene derivatives as sacrificial templates. Subsequently, the graphene template is eliminated through high-temperature annealing, allowing the metal atoms anchored on the template to be transferred onto the metal oxide support (figure 7(a)) [133]. The strong coordination of Pt SA on the surface of the metal oxide nanoparticles mitigates the risk of agglomeration, resulting in the thermally stable single atoms. The findings demonstrate the versatility of the sacrificial template method in the preparation of highly thermally stable SACs with a high loading capacity.

Yuan *et al* successfully synthesized N-doped hollow carbon spheres loaded with atomically dispersed Ni species (Ni(SA)/N-C) using SiO_2/polydopamine microspheres as the template. The Ni atoms were anchored by N atoms within the hollow microspheres, which were transferred from the polydopamine microspheres. The resulting Ni SACs (figure 7(e)) exhibited outstanding Faraday efficiency, stability, and selectivity for the electroreduction of CO_2 to CO, owing to the highly dispersed Ni single atoms and the unique hollow microsphere structure [173]. Similarly, Qiao *et al* synthesized Mn SACs supported on sulfur/nitrogen co-doped carbon (Mn(SA)/S–N–C) (figure 7(f)) by utilizing Mn ion-impregnated polypyrrole-coated cadmium sulfide (CdS) (CdS@Mn-PPy) as the template. The removal of the template was realized through a pyrolysis process, which synergistically acted with the evaporation of Cd atoms/clusters, leading to the formation of a hollow hierarchical porous structure. Meanwhile, the formation of a C–S–C bond could optimize the electronic structure of the Mn-N sites, leading to a significant improvement in the electrochemical performance of the Mn–N sites in the Li–S cell [134]. Additionally, inorganic materials such as MgO can also serve as templates for the synthesis of desired structures. Figures 7(g) and (h) depict the N-doped carbon-loaded nickel-nitrogen atoms (Ni(SA)/N_3–C) obtained using MgO as a template. It should be noted that the coordination environment of the Ni single-atom active site can be adjusted by controlling the pyrolysis temperature.

In addition to the type of template, the structure of the template also plays a significant role in determining the morphology of the resulting material and the dispersion of the metal atoms. For example, Zhang *et al* investigated the influence of the pore structure of the template on the synthesis of SACs by utilizing three different types of SiO_2 templates (MCM-41, SBA-15, and FDU-12) with distinct microstructures [175]. It was observed that the pore size of the template should fall within a suitable range to achieve atomically dispersed Co. When the pore size is smaller than the metal precursor (i.e. in the case of MCM-41 with a pore size of 2.66 nm), the metal precursor can only be adsorbed on the surface of the template and subsequently agglomerate during the pyrolysis process. In contrast, when the pore size is significantly larger, as seen in the case of FDU-12 with a pore size of 17.20 nm, there is a diminished constraining and anchoring effect on the Co complexes during pyrolysis, leading to the formation of Co clusters. Therefore, the achievement of atomically dispersed Co SACs (figure 7(i)) is realized by employing templates with appropriate microstructures, such as SBA-15 with a pore size of 11.10 nm. The resulting Co SACs exhibit excellent catalytic activity for the hydrodeoxygenation of lignin-derived species as well as the hydrogenation of various nitroaromatics.

In summary, the sacrificial template method offers two key advantages that contribute to the high activity of SACs. Firstly, it enables an improvement in the loading of single atoms, which enhances the catalytic performance. Secondly, it allows for a large exposure of the active sites to the gas phase, further enhancing the reactivity of the SACs. Moreover, this method is applicable to various support materials, including metallic, metal oxide, and perovskite nanosheets. However, despite these advantages, the sacrificial template method still faces certain limitations. On one hand, the synthesis process is more complex compared to other methods, requiring

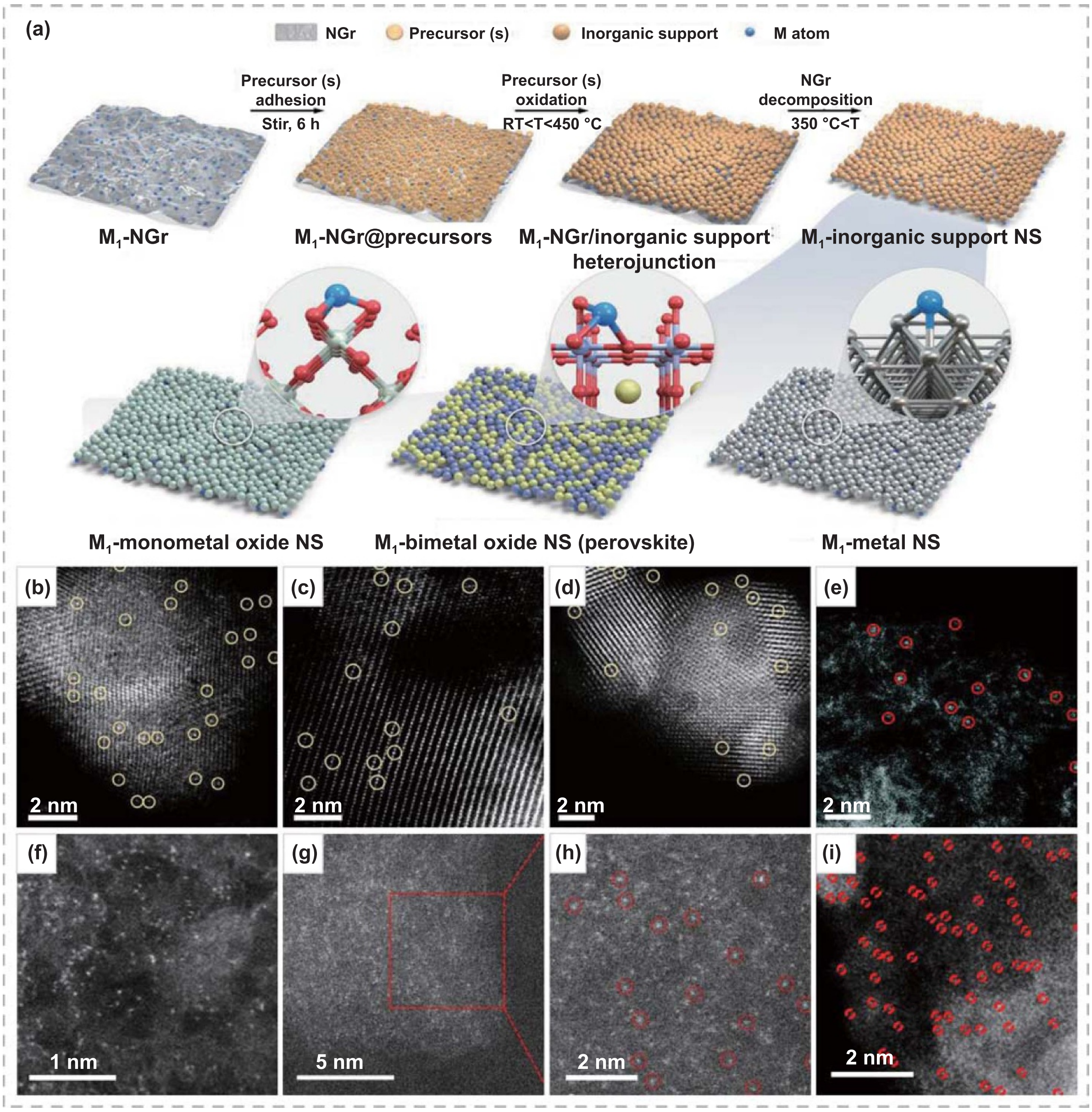

Figure 7. Preparation of SACs via sacrificial template method. (a) Schematic illustration for the synthesis of Pt SACs stabilized on various inorganic nanosheets (metal oxide, perovskite, and metallic) using the N-doped graphene sacrificial template route. (b)–(d) HAADF-STEM images of the Pt(SA)/SnO_2 NSs, Pt(SA)/NSs, and Pt(SA)/Pd NSs, respectively [133]. John Wiley & Sons. © 2021 Wiley-VCH GmbH. (e) HAADF-STEM image of Ni(SA)/N-C samples. Reproduced from [173] with permission from the Royal Society of Chemistry. (f) AC HAADF-STEM image of Mn(SA)/S-N-C. Reprinted with permission from [134]. Copyright (2022) American Chemical Society. (g) AC HAADF-STEM image and (h) enlarged image of Ni(SA)/N_3-C [176]. Reprinted from [176], © 2022 Elsevier B.V. All rights reserved. (i) HRTEM image of Co(SA)/N-C. Reprinted with permission from [175]. Copyright (2020) American Chemical Society.

careful consideration of multiple factors. On the other hand, the selection of a suitable sacrificial template is crucial, as it must effectively carry both the metal atom precursors and the support materials. Therefore, the future development of this method lies in the design and precise regulation of sacrificial templates tailored to the specific target SACs, with the aim of improving both the loading and activity of the SACs. The characteristics of the sacrificial template method, and other frequently used single-atom catalyst synthesis methods have been summarized in table 1.

3.7. Other synthesis methods

Apart from the methods mentioned above, various synthesis strategies with specialized pathways have been explored. These strategies, each with unique advantages, aim to address certain shortcomings associated with current SAC preparation methods, including low yield, aggregation, instability, complicated synthesis processes, and environmental pollution. Among these strategies, the absence of a universal method for controllable preparation of SACs with high surface metal

Table 1. The characteristic of different synthesis methods.

Method	Load capacity/wt%	Particle size	Advantage	Disadvantage
Impregnation	RhRu(SA)/SP-ZSM 1.12 [87] pT(SA)/hNCNC 1.96 [125]	0.78/0.7 nm [87] SA [125]	Simplicity of operation and low cost; appropriate for fabricating single-atom catalysts on some carriers with nanostructures	Low metal loading; easy aggregation
Co-precipitation	Ru(SA) /FeO$_x$ 0.18 [149] Ni(SA)/MgO 1 ~ 10 [150] Cu(SA)/SiO$_2$ 15 [151]	0.6 nm [149] SA [150] SA [151]	Simple procedure and short experimental period; high catalytic performance of the product	Low metal loading; some atoms may hide in the substrate; a mixture of different metal states
One-pot pyrolysis	Co(SA)/N-C 2.16 [152] Ni(SA)/N-CNT 20.3 [128]	SA [152] 0.15 nm [128]	Suitable for fabricating single-atom catalysts with high activity and loading	High reaction temperature and energy consumption; most metals tend to agglomerate at high temperatures
Atomic layer deposition	Pd(SA)/graphene 0.25 [132] Pt(SA)/N-graphene 2.1 ~ 7.6[162] Pt(SA)/graphene 1.52 ~ 10.5[163] Pt(SA)/N-C 0.8 ~ 10.5 [164] Cu(SA)/Al$_2$O$_3$ 0.5 ~ 2.0 [165]	SA [132] SA [162] SA-4 nm [163] SA-2 nm [164] SA-9.6 nm [165]	Great controllability and repeatability; appropriate for fabricating single-atom catalysts on some carriers with nanostructures	Low load capacity; high cost; easy to aggregate into clusters and nanoparticles
Sacrificial template	Pt(SA)/LaCoO$_3$ NSs 3.94 [133] Pt(SA)/SnO2 NSs 2.12 [133] Pt(SA)/Pd NSs 3.22 [133] Co(SA)/N-C 3.2 [175] Ni(SA)/N$_3$-C 0.84 ~ 1.82 [176]	SA [133] SA [175] SA [176]	High thermal stability; High loading capacity of single atoms	Available to specific systems; complex synthesis process
MOF-derived	Co(SA)/N-C 4 [166] Fe(SA)/N-C 2.16 [167] Pt(SA)/Ce-MOF 0.12 [168] Fe(SA)/N-C 0.94 [172] Rh(SA)/ZSM-5-H 0.45 ~ 0.71 [135]	SA [166] SA [167] SA [168] SA [172] SA [135]	High scalability; high thermal stability	The requirement of high-temperature-treatment; low loading capacity;

densities and high productivity remains a significant hurdle in the pathway to the industrialization of SACs. Recently, Hai *et al* proposed a general method to realize atomic-level dispersion of 15 types of metal atoms with loadings up to 23 wt% on different supports. This method combines impregnation with a two-step annealing process (figures 8(a) and (b)). For effective anchoring of the metal precursor and the controlled removal of the ligand, it is crucial that the temperature of the first annealing step (T1) remains lower than the decomposition temperature of the metal precursor. Subsequently, a second annealing at a higher temperature (T2) is performed to remove the chemisorbed metal precursor, while simultaneously converting the remaining ligand into single atom. The simulation and experimental results have revealed the synthesis mechanism at the molecular level. It is the controllable removal of ligands and the interaction between the metal precursor and the support that prevents the thermally induced aggregation of atoms into nanoparticles effectively [124]. The synthesis strategy is simple in operation and can be easily extended to a large-scale preparation. Meanwhile, it presents a novel approach by combining different methods for the synthesis of SACs.

Usually, metal atoms with high dispersion tend to migrate and agglomerate due to their high surface energy, resulting in poor stability. To address this issue, Zeng *et al* designed a catalyst of the ‘nanoglues’ type, where the active metal atoms are isolated on separated islands. These SACs can freely move within their respective islands but are prevented from migrating across the islands, thereby realizing a dynamically stabilized atom configuration. Initially, high-density $[\mathrm{Ce(OH)}_x]^{y+}$ species were attached to the silicon oxide surface through liquid-phase electrostatic adsorption (LPE) synthesis. After calcination, uniformly dispersed and isolated CeO_x nanoclusters were formed. Subsequently, the Pt SACs were precisely placed on these ‘nano-islands’ by LPE again, guided by the principle of the zero electric point (figure 8(c)). As a result, the Pt atoms remain dispersed in both oxidizing and reducing environments at high temperature, exhibiting significantly enhanced catalytic activity for CO oxidation [177]. This study presents a novel approach to address the inherent

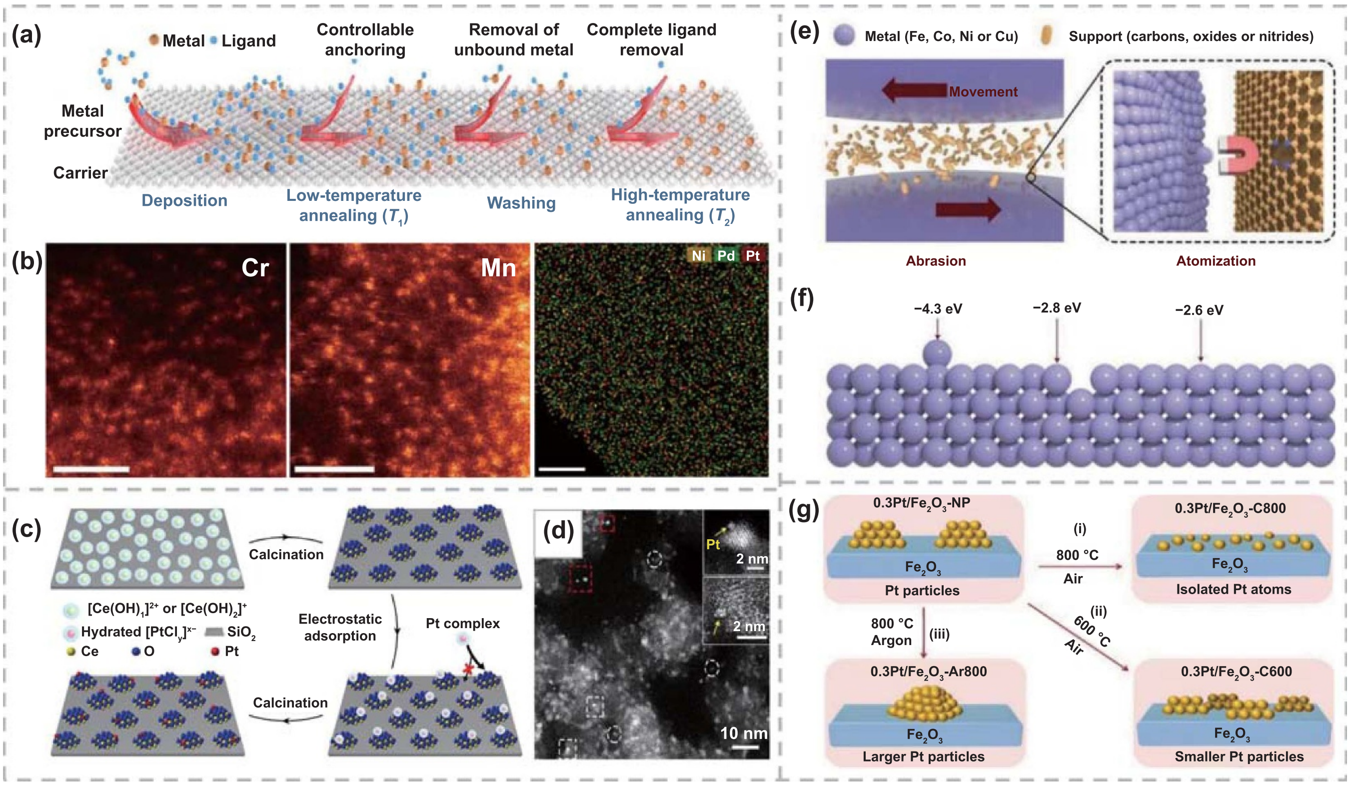

Figure 8. Preparation of SACs via other methods. (a) Strategy of scalable two-step annealing method for the preparation of ultra-high-density SACs. (b) Atomic-resolution annular dark-field scanning transmission electron microscopy (ADF-STEM) images of various metals on nitrogen-doped carbon support. All scale bars are 1 nm. Reproduced from [124], with permission from Springer Nature. (c) Schematic diagrams illustrating the fabrication processes of functional CeO_x nanoglue islands and CeO_x/SiO_2-supported Pt SACs. (d) HAADF image of a high-loading Pt(SA)/CeO_x-SiO_2 catalyst. Reproduced from [177], with permission from Springer Nature. (e) Schematic of the mechanism for the top-down abrasion method obtaining SACs. (f) Comparison of segregation energy (ΔE_{seg}) for Fe SA (purple spheres in figure) captured by N–C moieties at different sites. Negative energy indicates released energy. Reproduced from [178], with permission from Springer Nature. (g) Illustration of thermally induced Pt nanoparticle restructuring. Reproduced from [179]. CC BY 4.0.

trade-off between catalytic activity and stability. Moreover, the utilization of functional nano-islands to ensure the atomic-level dispersion of various metals offers a promising strategy, making the 'nanoglues' catalyst applicable to a wide range of reactions. This advancement holds tremendous potential for diverse applications in the field.

The aforementioned methodologies not only entail considerable complexity but also tend to yield unnecessary hazardous waste products. To simplify this process, Han *et al* introduced a ball milling technique [178]. This method involves the direct atomization of bulk metals, such as iron, cobalt, nickel, and copper, onto various supports through a top-down milling approach. The outcomes of density functional theory (DFT) calculations elucidate the mechanism behind the transformation of metal particles into single atoms during ball milling, as depicted in figures 8(e) and (f). Using iron as an illustration, the repetitive collisions of iron balls convert mechanical energy into structural disorder, inducing surface defects on both the iron balls and the supporting materials [178]. The activated iron surface serves a dual role, functioning not only as a catalyst for nitrogen dissociation but also in the formation of Fe–N–C. In comparison to other metals, nitrogen-doped graphitic nanoparticles exhibit a high segregation energy (ΔE_{seg}, −4.3 eV, as depicted in figure 8(f)) due to the robust Fe–N bonds, facilitating the facile detachment of atoms from the iron spheres. Consequently, metal atoms are generated, activating the metal ball surface. Subsequently, the catalytic effect of the activated metal surface induces the decomposition of surrounding nitrogen into N atoms, which, in turn, are incorporated into the defective supports, enhancing the anchoring of metal atoms. Therefore, the metal atoms are captured and stabilized by the N-doped supports. Nitrogen atoms here can inhibit the aggregation of individual metal atoms into clusters on the support surface. Importantly, the loading of single atoms can be finely tuned by adjusting milling parameters, offering an efficient and environmentally friendly approach for the preparation of SACs.

Isolated atoms on the support in SACs are typically stabilized by various defects [90, 120, 133]. However, achieving high metal loading and thermally stable SACs poses a challenge, primarily due to the difficulty in generating high-density defects. To tackle this challenge, Lang *et al* proposed a method involving the transformation of Pt nanoparticles into a single-atom dispersed state on defect-free Fe_2O_3 surface through high-temperature calcination, as illustrated in figure 8(g). Three conditions are requisite for this process: high temperature (facilitating increased Pt atom mobility), the presence of molecular O_2 (oxidizing the Pt NP surface), and robust interactions between the support and Pt atoms. Notably, the reducibility of Fe_2O_3 is imperative for establishing strong interaction between Pt SA and the Fe_2O_3 support in this method [179]. This defect-free stabilization strategy can be extended to irreducible supports, such as perovskites and spinels, by simply doping iron oxides into them. This approach opens a new avenue for the fabrication of highly loaded SACs applicable to various industrial catalytic reactions.

4. How does SACs improve the sensing performance

Since the excellent catalytic properties of SACs, it is expected to greatly promote the response of gas sensors if SACs are taken as the sensitive materials compared with the conventional sensitive materials [80, 99]. Two fundamental aspects contribute to the augmented responsivity of SACs towards target gases. On the one hand, the extensive electron transfer between the SACs and target gas molecules induces a change in the conductivity of sensitive materials, influencing sensing performance and amplifying the response. On the other hand, the support material hosting the single atoms plays a crucial role in shaping the electronic structure, size, morphology and thermal stability of single atoms materials, thereby affecting the catalytic activity and selectivity of the sensing materials [64].

4.1. Interaction between SACs and gas molecules

Upon the interaction between SACs and target gas, the adsorption, activation, and electron transfer can be effectively improved. The heightened response and sensitivity of the gas sensor can be elucidated through four key aspects.

4.1.1. More chemisorbed oxygen. The single atom functions as the active site, enhancing the adsorption of oxygen from the air and facilitating the dissociation of oxygen molecules into oxygen ions. The oxygen species generated at the active site will diffuse to other regions of the material (named spillover effect), leading to a substantial increase in the quantity of active oxygen on the surface of the support materials (figure 9(a)) [54]. Take the Au-sensitized ZnO nanorods structure as an example, Au SA may serve as the specific adsorption site for the dissolution of oxygen molecules, followed by the spillover of larger quantities of oxygen ionic species (O^{2-}) on the ZnO surface and reaction with the target gas molecules [180]. Moreover, metal single atoms interact with oxygen atoms on the support, leading to the desorption of lattice oxygen from the support and the creation of oxygen vacancies, which may further promote the generation of adsorbed oxygen [81].

4.1.2. Enhanced amount of electron transfer. The dispersion of metallic atoms at the atomic level exposes numerous active sites, each demonstrating exceptional activity. The presence of individual active sites, coupled with single atom modification, effectively facilitates charge transfer between the sensitive materials and gas molecules. Liu *et al* systematically investigated the charge density difference of H_2S molecules adsorbed on the surface of pure In_2O_3, Pd(NP)/In_2O_3, PdO/In_2O_3 and Pd(SA)/In_2O_3 [80]. Although the electron transport occurred in all four structures (figure 9(b)), the number of electrons transferred from the H_2S molecule to the Pd atomic site ($\Delta q = 0.73e$) is larger than that observed on the other three sensing surfaces. More importantly, such strong electron transfer favors enhanced adsorption of H_2S gas and lengthens the S–H bond. This elongation is conducive to the dissociation of the H_2S molecule into HS species and sulfur species ($S^{\delta-}$). Subsequently, the $S^{\delta-}$ species will spill over to the adjacent surface of In_2O_3, leading the sensing layer to lose electrons and enhancing the resistance change of the Pd(SA)/In_2O_3 based sensor.

4.1.3. Improved gas adsorption energy. The sensitive materials modified with single atoms exhibit a pronounced affinity for gas molecules. It may increase the adsorption energy of the material for the target gas compared with the normal sensitive materials, leading to a larger change of the channel current, therefore, a higher sensitivity [82]. To elucidate the mechanism of Pt SA used to enhance the performance of $Ti_3C_2T_x$ for the detection of triethylamine (TEA) gas, Mao *et al* investigated the adsorption energy of TEA on various sites (OH^-, O^-, F^-) of $Ti_3C_2T_x$ by DFT simulation. The Pt(SA)/$Ti_3C_2T_x$ showed higher adsorption energies on all binding sites compared with pure $Ti_3C_2T_x$ and Pt(NP)/$Ti_3C_2T_x$. The higher adsorption capacity of Pt(SA)/$Ti_3C_2T_x$ for TEA induced more positive interactions between the gas molecules and the sensitive materials, leading to a higher sensitivity, faster response, and theoretically slower desorption [182].

4.1.4. Accelerated catalytic kinetics. The mechanism of most chemoresistive gas sensors is a catalytic process. The single atom dispersions demonstrate a higher intrinsic electrocatalytic capacity and faster catalytic kinetics in the reaction between the sensing material and target gas molecules compared to their nanoparticle counterparts. This heightened performance can be attributed to the unique electronic structures and unsaturated coordination environments of the single atom configurations [183]. Zhang *et al* calculated the changes in free energy and reaction energy barriers for all possible elemental hydrogen reduction steps in the redox reaction of methanol and oxygen on the Ag(SA)/$LaFeO_3$@ZnO—Pt surface (figure 9(c)). It is concluded that the introduction of Pt SA is found to significantly reduce the reaction energy barriers for methanol and oxygen ions on the surface of the sensitive material, which improves the sensitivity and selectivity of Ag(SA)/$LaFeO_3$@ZnO—Pt to methanol gas [181].

4.2. Interaction between SACs and their supports

The interaction between metal SACs and their supports also plays a decisive role in the enhancement of gas sensing properties. It is expected to be explained in the following four aspects.

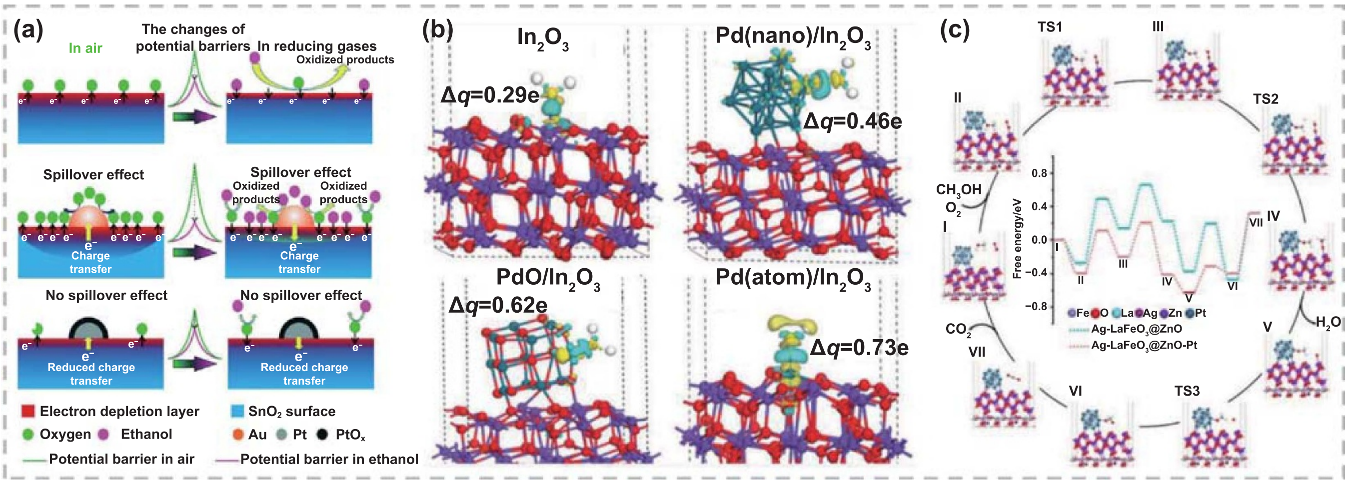

Figure 9. The interaction between the SACs and gas molecules. (a) Schematic diagram illustrating the sensitization mechanism of the spillover effect. Reproduced from [54] with permission from the Royal Society of Chemistry. (b) The different charge densities and corresponding Bader charge (Δq) of H_2S gas molecules adsorbed on pure In_2O_3, Pd(NP)/In_2O_3, PdO/In_2O_3, and Pd(SA)/In_2O_3, respectively. The yellow areas present the electronic dissipation regions, which stands for the electronic aggregation region [80]. John Wiley & Sons. © 2021 Wiley-VCH GmbH. (c) The mechanism of the oxidation reaction for methanol gas on the Ag(SA)/$LaFeO_3$@ZnO stabilizing the Pt single-atom sample (Ag(SA)/$LaFeO_3$@ZnO–Pt). The inset shows the activation energy of the ions and molecules of Ag(SA)/$LaFeO_3$@ZnO and Ag(SA)/$LaFeO_3$@ZnO–Pt at different reaction stages. Reprinted with permission from [181]. Copyright (2022) American Chemical Society.

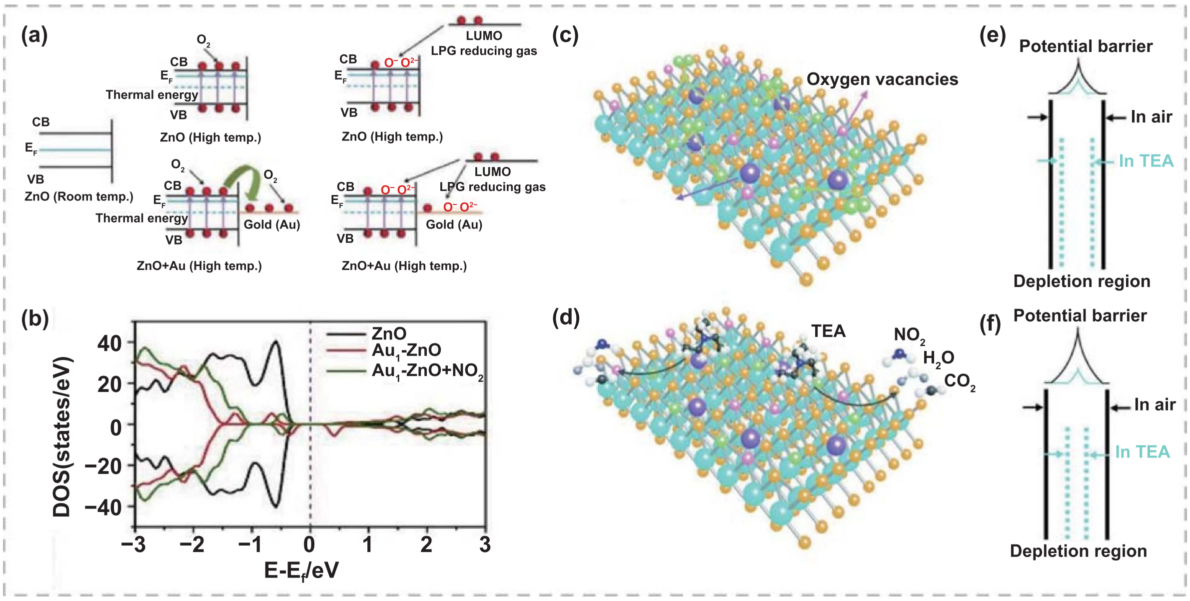

Figure 10. The mechanisms of interaction between SACs and their supports. (a) The schematic band diagram of pure ZnO nanorods, and ZnO nanorods sensitized with Au. Reprinted from [180], © 2016 Elsevier B.V. All rights reserved. (b) Calculated the density of states (DOS) diagram of ZnO, Au(SA)/ZnO, and Au(SA)/ZnO + NO_2. Reprinted from [90], © 2020 Elsevier Inc. The surface reaction mechanisms of Pt(SA)/SnO_2 thin films in (c) air and (d) TEA, the changes in the surface potential barrier and depletion layer thickness of (e) a SnO_2 thin film and (f) a Pt SA/SnO_2 thin film. Reproduced from [184] with permission from the Royal Society of Chemistry.

4.2.1. More available surface electrons. The difference of work function between the SA and its support leads to electron transfer between them [180]. Figure 10(a) draws an energy band of a composite material (Au sensitized ZnO nanorods) at high temperature, in which the electron in the conduction band of ZnO migrates to Au owing to the higher work function of Au. This migration results in an increased concentration of electrons distributed on the surface of the composite material (figure 10(a)) [180]. This effect contributes to the availability of more electrons for capturing oxygen from the atmosphere. More absorbed oxygen means that more captured electrons will be released back into the conduction band when it is exposed to reducing gases, therefore resulting in a higher response to target gases.

4.2.2. Higher initial resistance. The doping effect of SA will change the conductivity of the support material both in air and in the target gas. The doping of SA will cause the formation of heterojunctions [78, 79, 185] and Schottky junction [79], thereby increasing the initial resistance of supports. The Pt SA doping results in a thicker depletion region and higher potential barrier compared with the initial SnO_2, the black line denotes the potential barrier and depletion region in air and the cyan one in TEA atmosphere in figures 10(e) and (f). As shown in figure 10(b), it is evident that Au atom doping broadens the bandgap of ZnO, consequently increasing the resistance of the sensing material [90]. The synergistic effect of higher initial resistance and more electrons released by the target gas results in a more pronounced variation in resistance when the sensing materials are transferred from atmosphere to target gas (figures 10(e) and (f)) [184], i.e. an enhanced response to the target gas.

4.2.3. Accelerated electron transfer. The Schottky barrier plays a crucial role in expediting electron transfer between the SA and its support material due to the built-in electric field [65, 79, 186]. Chen *et al* revealed that the existence of Pt-O-Ti^{3+} atomic interface can accelerate the transfer efficiency of photogenerated electrons from Ti^{3+} sites to Pt atoms through photoelectrochemical characterizations and DFT calculations. The accelerated electron transfer facilitates the sensing material in promptly responding to changes in gas concentration, resulting in shorter response and recovery times.

4.2.4. Enhanced thermal and chemical stability. The electron transfer between the metal SA and the support can also aids in anchoring the SA, thereby contributing to the enhanced thermal and chemical stability of the single atoms [92, 164]. For example, the chemical stability of Co(SA)/N-C is much higher than that of Co(NP)/C. This is due to the fact that Co-N_3 is highly dispersed on the carbon matrix, which minimized the Co leaching [153]. On the other hand, stronger support-SA interactions can also enhance the thermal stability of the materials. The thermal stability of Ni SAC loaded on Ce-doped hydroxyapatite (HAP) support (Ni(SA)/Ce-HAP) is significantly higher than that on pristine HAP support (Ni(SA)/HAP). This stability is attributed to the cerium doping, which stabilizes the atomically dispersed Ni even at high temperatures through a heightened metal-support interaction. As a result, Ni(SA)/Ce-HAP shows a modest decrease of 10% for the CO_2 conversion rate at 750 °C over 65 h. For comparison, the CO_2 conversion of Ni(SA)/HAP went through rapid deactivation, decreasing by 17% over only 7 h under the same condition [187].

5. The application of SACs in gas sensing

SACs have been widely used for the detection of various gases including ammonia, hydrogen sulfide, nitrogen dioxide, sulfur dioxide, volatile organic compounds, etc., due to their unique sensitizing effect. As described in section 4, the enhancement of gas sensitization performance of SACs as sensitive materials can be accomplished by the promotion of the adsorption, activation, and electron transfer of gas molecules by single atoms. Consequently, the specific type of gas becomes a crucial consideration in the design of SACs as sensitive materials. In this section, we consolidate and summarize the gas-sensitive performance of SACs currently employed for various gas detections, categorized by gas type. This compilation serves as a valuable reference for the tailored design of SACs intended for diverse gas detection applications.

5.1. Ammonia

Given its high volatility and toxicity, elevated concentrations of ammonia (NH_3) pose a significant risk, causing severe damage to the skin and respiratory system. Beyond its hazards, ammonia finds extensive application in the chemical industry for synthesizing various materials and holds potential as an energy carrier for future automobiles. Additionally, ammonia serves as a diagnostic marker in the exhaled breath of individuals with lung and kidney diseases, offering potential for early disease detection. Consequently, establishing an effective method to detect low concentrations of NH_3 is essential for practical applications, encompassing both safety considerations and diagnostic advancements [188].

Tian *et al* prepared atomically dispersed Co SA (figure 11(a)) on the N-doping carbon matrix (Co(SA)/N-C) by calcining a cobalt (II) complex. The STEM image (figure 11(a), red circles) proves the atomic and uniform distribution of Co SA on the matrix [103]. The NH_3 sensor using Co(SA)/N-C as the sensitive material shows a high responsivity of 1.21–20 ppm NH_3 at room temperature (figure 11(b)). Furthermore, a variety of gases including C_2H_5OH, CH_4, CO_2, H_2, NO_2, and NO were measured at room temperature with the same concentration (200 ppm) (figure 11(c)). The response to NH_3 is notably higher than that observed for comparison gases. This heightened sensitivity can be attributed to the stronger affinity of Co(SA)/N-C for nitrogen-containing gas molecules such as ammonia or other organic amino gases. In contrast, for other Co-doped oxide sensors (not Co SA), the detection limit for NH_3 is approximately 50 ppm at room temperature (figure 11(d)) [189], which proves the advantage of SACs for gas sensing in return. The sensing mechanism is attributed to the catalysis of Co SACs for ammonia oxidation reaction on the surface of Co(SA)/N-C. The unique electronic structure and unsaturated coordination environment of Co SACs contribute to a lower activation energy and higher reaction rate. As a result, the catalytic activity of Co SACs proves essential in achieving a low detection limit for NH_3 at room temperature.

5.2. Hydrogen sulfide

Hydrogen sulfide (H_2S) is a gas characterized by a potent odor and significant danger. Exposure to high concentrations of H_2S can result in shock, respiratory distress, and even coma. Moreover, H_2S plays crucial physiological and pathological

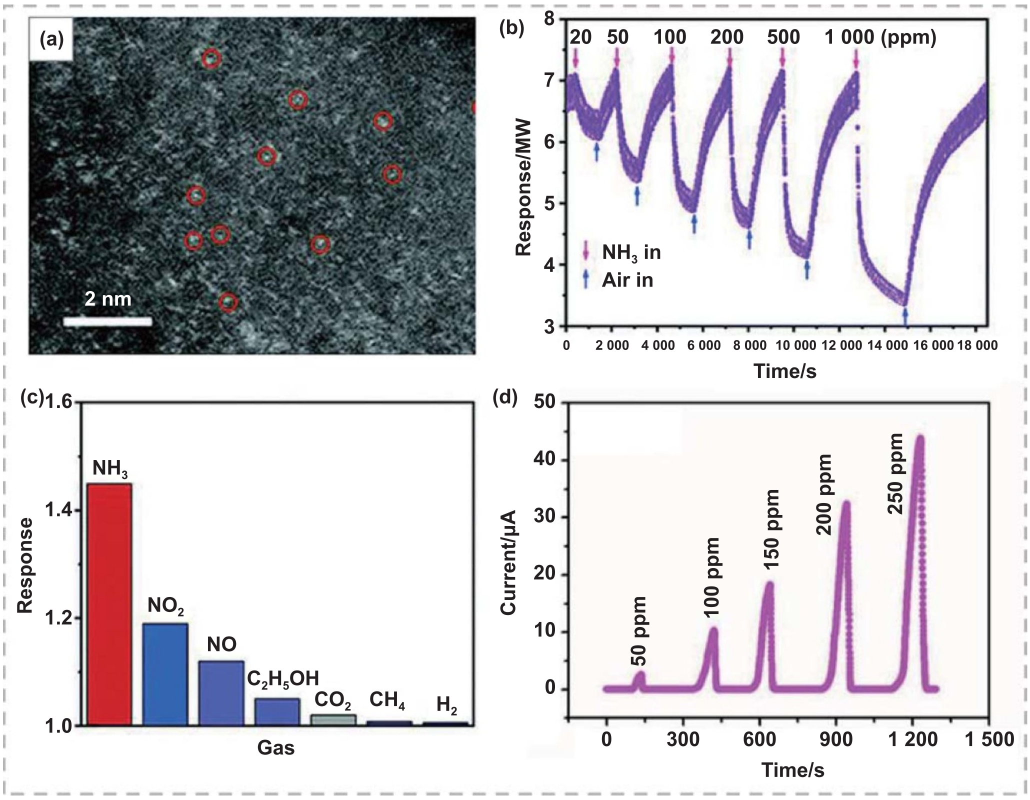

Figure 11. The applications of SACs in NH_3 sensing. (a) AC HAADF-STEM image of the single Co atom on the N-doping carbon matrix (Co(SA)/N-C). (b) Response curve of Co(SA)/N-C based gas sensor to NH_3 from 20 ppm to 1000 ppm at room temperature. (c) The response contrast of Co(SA)/N-C based gas sensor to various gases (NH_3, NO_2, NO, C_2H_5OH, CO_2, CH_4 and H_2) at 200 ppm. Reproduced from [103] with permission from the Royal Society of Chemistry. (d) The response of Co-doped MoO_3 thin films based gas sensor to NH_3. Reprinted from [189], © 2022 The Author(s). Published by Elsevier B.V.

roles in living systems. Given these factors, detecting H_2S at low concentrations is of paramount importance for human life and health, ensuring timely identification and prevention of potential hazards.

Pd is a face-centered cubic metal. Pd SA demonstrates exceptional catalytic ability, effectively enhancing the adsorption and dissociation of gas molecules in gas detection applications. Its remarkable chemical stabilization and selectivity make it particularly effective for gases such as H_2 and H_2S [190]. The indium (III) oxide (In_2O_3) is one of the most effective sensitive materials for H_2S detection, which can detect H_2S even at ppb level [191]. Liu *et al* synthesized Pd(SA)/In_2O_3 with high stability by MOF-derived method. The response of Pd metal to hydrogen sulfide at different sizes is shown in figure 12(a), where the magnitude of the response values is ranked as follows: Pd(SA)/In_2O_3 $>$ Pd(NP)/In_2O_3 $>$ In_2O_3, indicating that the loaded Pd SACs greatly improves the gas response. Moreover, the response comparison to different gases (figure 12(b)) demonstrates that the loading of Pd SACs increases the selectivity of the sensitive material for H_2S by decreasing the sensitivity to interfering gases such as CH_3SH. This is because that the adsorption energy of the Pd SA site for H_2S molecules is -3.63 eV. The value is much lower than that of CH_3SH and other molecules (figure 12(c)), leading to an easier adsorption of H_2S onto Pd(SA)/In_2O_3 [80]. The sensing mechanism of Pd(SA)/In_2O_3 can be described by following equations (2)–(4). The Pd SACs can promote the dissociation of chemically adsorbed H_2S molecule into $^*HS$ firstly, which will further decompose into $S^{\delta-}$ species. The formed $S^{\delta-}$ species subsequently diffuse to the surface of In_2O_3 surrounding the Pd atom, where they react with chemically adsorbed O^{2-}. The electrons released from the $S^{\delta-}$ species return to the conduction band of In_2O_3, thereby amplifying the current in the gas sensor. This increase in current serves as an indicator of the presence of H_2S

$$H_2S \rightarrow H^* + {}^*HS \tag{2}$$

$$^*HS \rightarrow S^* + H^* \tag{3}$$

$$S^{\delta-} + O_2^- \rightarrow SO_2(\text{gas}) + (\delta+1)e^- \tag{4}$$

In addition, Pt catalysts are extensively employed in gas sensors owing to their high activity and stability. In an effort to enhance the utilization of Pt atoms, Zhang *et al* fabricated a range of isolated Pt SA-anchored $CuCrO_2$ (Pt(SA)/CCO) with varying loadings using a glycine-nitrate solution combustion synthesis method [89]. The Pt SACs density can reach a peak of $\sim$100 μm^{-2} at the loading of 1.39 wt%. The Pt anchored CCO steadily promotes the response characteristics to H_2S, exhibiting an improved response to H_2S of 10 ppm–1 250 ppm at a low temperature of 100 °C, which is 35 times higher than that of pure CCO (figures 12(d) and (e)). Furthermore,

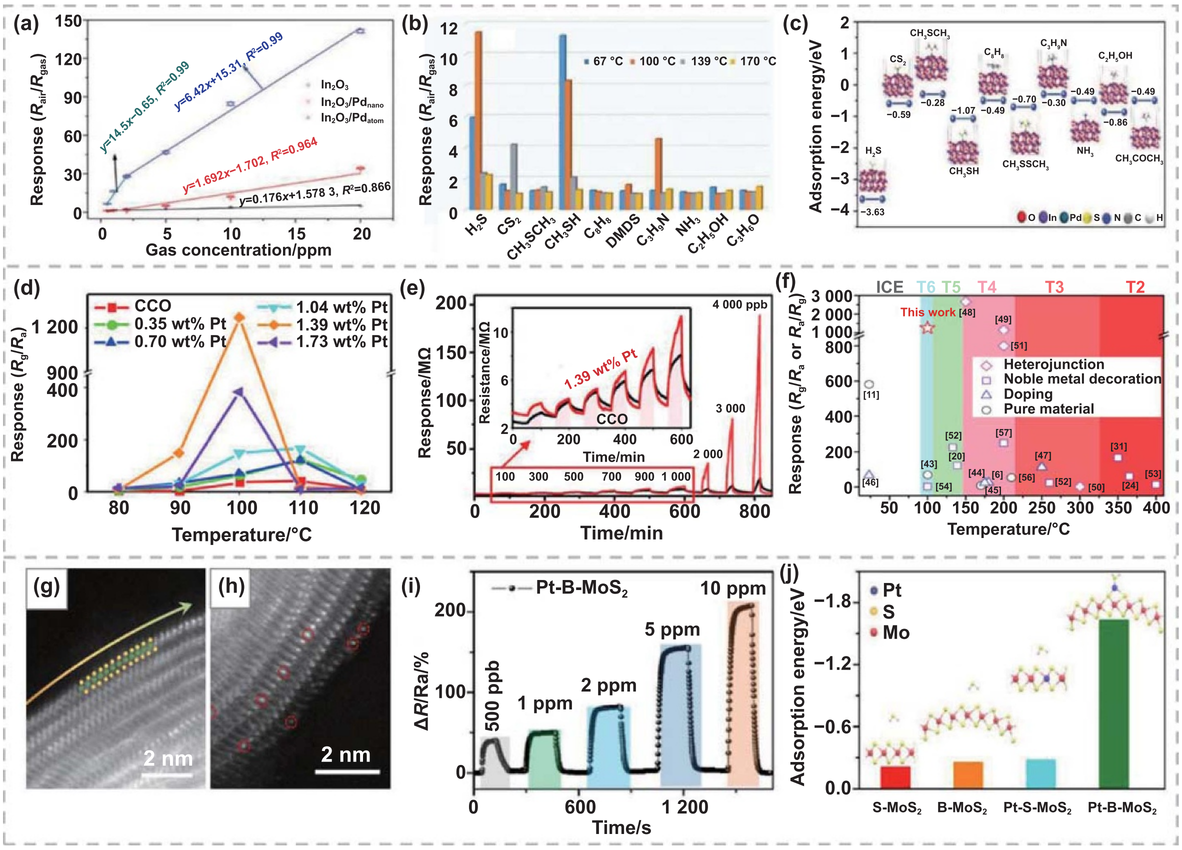

Figure 12. The applications of SACs in H_2S sensing. (a) The responses of pure In_2O_3, Pd(SA)/In_2O_3 and Pd(NP)/In_2O_3 based H_2S sensors, respectively. (b) The response contrast of Pd(SA)/In_2O_3 based sensors to various gases. (c) The adsorption energy (E_{ads}) comparison of Pd(SA)/In_2O_3 surface toward different gas molecules [80]. John Wiley & Sons. © 2021 Wiley-VCH GmbH. (d) The response of sensors based on pure CCO and Pt(SA)/CCO with different Pt loadings to 10 ppm H_2S at 80 °C–120 °C, respectively. (e) The response of sensors based on CCO and 1.39 wt% Pt(SA)/CCO to 100–4000 ppb H_2S at 100 °C. (f) The comparison of response and operating temperature of the various H_2S chemiresistors to 10 ppm H_2S. Reprinted with permission from [89]. Copyright (2022) American Chemical Society. (g) The HAADF-STEM image of the B-MoS_2 sample and (h) Pt(SA)/B-MoS_2 sample. (i) The time-related dynamic responses of Pt(SA)/B-MoS_2. (j) The H_2S-adsorption models and adsorption energy of S-MoS_2, B-MoS_2, Pt(SA)/S-MoS_2, and Pt(SA)/B-MoS_2 samples, respectively. Reproduced from [192]. CC BY 4.0.

figure 12(f) compares the sensing performance of Pt(SA)/CCO based sensor and other chemiresistors for H_2S detection, in which the former shows high response and high selectivity at a relatively low operating temperature. The *in-situ* characterization reveals that the mechanism of the material's sensitivity to H_2S is mainly the spillover catalytic effect of the Pt SACs, which includes the conversion of O^{2-} to the more reactive O^- ion and the simultaneous dissociation of the H_2S molecule into SH radicals and H atoms. These effects collectively promote the redox reaction between the adsorbed oxygen species and the SH radical on the material surface (equation (5)), thereby increasing the electrical response of the sensor

$$2SH_{(ad)} + 5O^-_{(ad)} \rightarrow 2SO_{2(ad)} + H_2O_{(ad)} + 5e^-. \quad (5)$$

Moreover, Li *et al* elevated the performance of their H_2S sensor through strain-assisted immobilization of Pt SA on the curved surface of MoS_2. The HAADF-STEM image in figure 12(g) manifests that the bent MoS_2 (B-MoS_2) is highly curved at the atomic scale with interconnected fullerene spheres supporting the high-quality MoS_2 surface. After introducing Pt into the B-MoS_2 surface, the HAADF-STEM image (figure 12(h)) clearly indicates that the isolated Pt atoms are uniformly distributed on the B-MoS_2 surface without obvious agglomeration. As a result, the Pt(SA)/B-MoS_2 sensor exhibits cyclically stable dynamic response and recovery characteristics at different concentrations of H_2S (figure 12(i)) [192]. Finally, DFT calculations elucidate the mechanism behind the substantial improvement in gas adsorption resulting from the introduction of a curved structure and Pt SACs (figure 12(j)). The high curvature of the MoS_2 surface induces 0.8% tensile strain on a single Pt site with low coordination, attributed to a unique 'tip' effect. This effect accelerates the electrical transfer process between H_2S and the support, ultimately leading to a significant enhancement in the sensing response.

5.3. Nitrogen dioxide

The presence of nitrogen dioxide (NO_2) in the air, even at low concentrations, can inflict irreversible damage to the human respiratory system and lead to respiratory diseases [193]. In addition, nitrogen dioxide can function as a biomarker for the non-invasive detection of pneumonia [194]. Thus, accurate

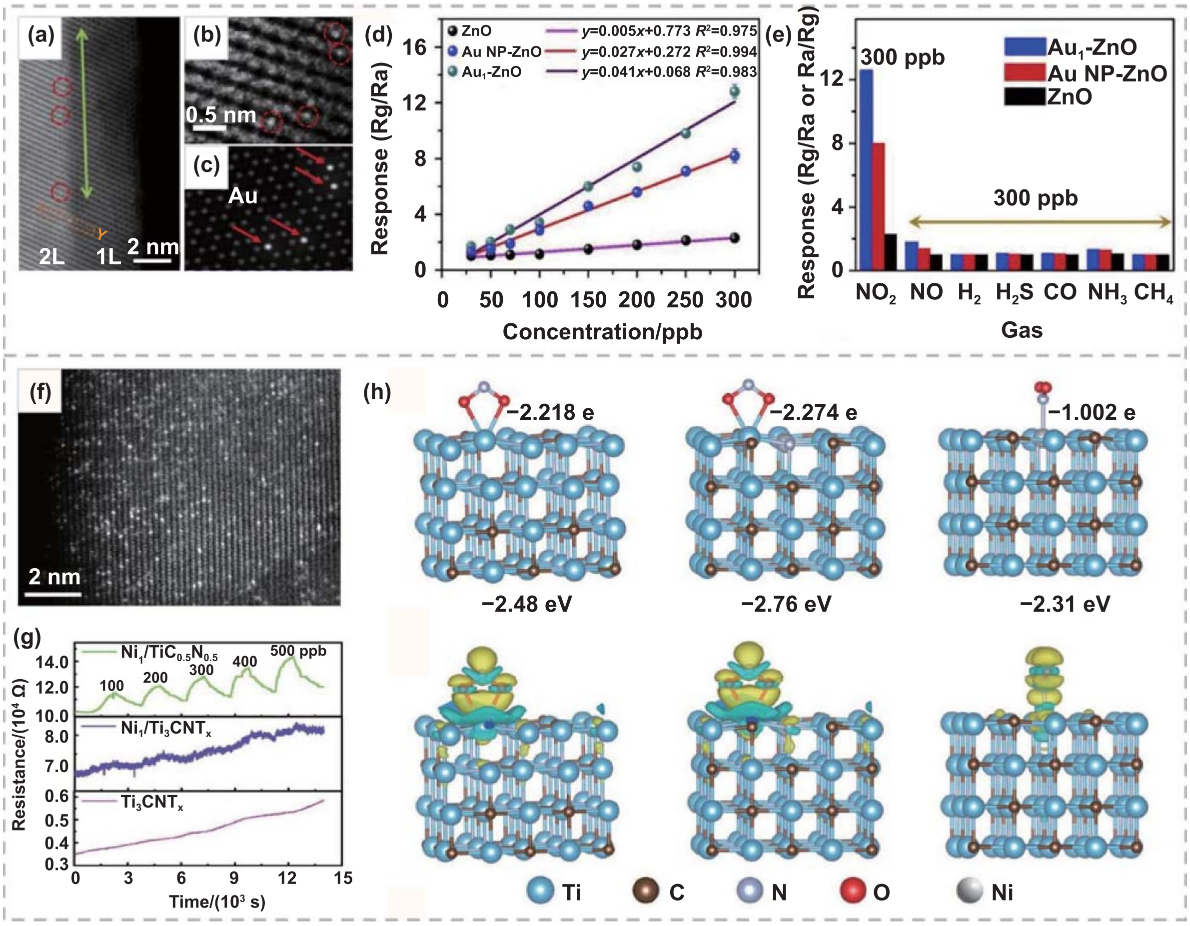

Figure 13. The application of SACs in NO_2 sensing. (a) HAADF-STEM image of Au(SA)/ZnO. (b) and (c) HAADF-STEM image of Au(SA)/ZnO and its simulated image. (d) The gas-sensing responses in different NO_2 concentrations for pristine ZnO, Au(NP)/ZnO, and Au(SA)/ZnO. (e) Selectivity of ZnO, Au(NP)/ZnO, and Au(SA)/ZnO toward various analyte gases. Reprinted from [90], © 2020 Elsevier Inc. (f) AC-HADDF-STEM images of Ni(SA)/$TiN_{0.5}C_{0.5}$. (g) Dynamic sensing transients to different NO_2 concentrations based on Ni(SA)/$TiN_{0.5}C_{0.5}$, Ni(SA)/Ti_3CNT_x, and Ti_3CNT_x. (h) The optimized NO_2 adsorption geometries and corresponding differential charge densities on perfect $TiN_{0.5}C_{0.5}$(200) surface, Ti atoms of Ni(SA)/$TiN_{0.5}C_{0.5}$ surface and Ni atoms of Ni(SA)/$TiN_{0.5}C_{0.5}$ surface, respectively. Reproduced from [196], with permission from Springer Nature.

detection of NO_2 is crucial for both environmental monitoring and medical diagnosis. Presently, the primary method involves chemiluminescence, but it has drawbacks such as high cost and non-real-time detection. Consequently, there is an urgent need for the development of portable, highly sensitive gas sensors capable of real-time NO_2 detection.

Au atoms loaded on ZnO surface (Au(SA)/ZnO) were used as the sensitive material to detect NO_2 in the range of 12.6 ppb–300 ppb. The Au atoms were stabilized by the unsaturated step defects (figure 13(a)), resulting from the layer-by-layer growth during ZnO crystal formation [90]. The individual Au atoms in the Au(SA)/ZnO can be seen explicitly in HAADF-STEM image (figure 13(b), red circle). The higher availability of Au SACs to the gas molecules makes the sensing material much more responsive to NO_2 molecules compared to Au(NP)/ZnO and ZnO (figure 13(d)). The exceptional sensing performance arises from the robust interaction between the gas molecule and the sensitive material. Upon exposure to NO_2, the Au atoms play a pivotal role as chemical sensitizers, facilitating the chemical reaction between NO_2 and adsorbed oxygen. Simultaneously, these Au atoms promote electron transfer between gas molecules and the support material. According to DFT calculations, there is a substantial amount of electron transfer (0.68e) from Au(SA)/ZnO to the NO_2 molecule after gas molecule adsorption. In comparison, the corresponding charge transfer for Au(NP)/ZnO and ZnO is only 0.51 and 0.06, respectively. The stronger electron transfer can explain the greater sensitivity of Au(SA)/ZnO to nitrogen dioxide. Moreover, the presence of Au atoms promotes the selectivity of the sensing material towards NO_2, compared with that of Au(NP)/ZnO. The response of Au(SA)/ZnO to the target gas molecules increases by around 56%, while the response to interfering gases contains almost the same as other interfering gases (figure 13(e)) [90]. Furthermore, recent work published by Zhang *et al* elucidates the impact of the size effect of Pt sensitization on NO_2 gas sensing. Fine control of size and loading of the Pt species on the ZnO nanowires was achieved through ALD and solution methods. As the number of ALD cycles increased, the size of Pt particles grew from a single atom to an average of 11.86 nm. Interestingly, this increase in size was accompanied by a decreasing trend in sensor resistance. The nanowire sensor with moderate Pt loading (0.61 at%) and a size of 3.95 nm showed an optimal response to NO_2 from 7.01 ppm to 20 ppm NO_2, which has a 5-fold enhancement compared to pristine ZnO [195].

Apart from metal-oxide semiconductors, other materials can also exhibit a significant enhancement in their gas-sensitive properties with the SACs modification. For example, atomically dispersed Pd cations loaded on CdSe quantum dot gels (Pb(SA)/CdSe QD) were synthesized to detect NO_2 at room temperature. The optimal combination of high response and fast recovery was achieved when the Pb SA loading reached its highest level (the atomic ratio of Pb: Cd was 0.09: 0.91), showing excellent performances with extremely low limit of detection (3 ppb), high sensitivity ($0.06\%\cdot ppb^{-1}$), short response ($\sim$28 s) and recovery time ($\sim$60 s). The high performance can be attributed to two aspects: one is the intrinsic porous structure of the gel, which promotes the accessibility of active sites to NO_2; the other is the highly decentralized Pb cations, which facilitates electron transfer between the Cd cations and the NO_2 molecules [194].

Single atoms loaded on the 2D materials can also be used to detect NO_2. For example, the *in-situ* doping of Ni atoms on the MXenes analog $TiC_{0.5}N_{0.5}$ (Ni(SA)/$TiN_{0.5}C_{0.5}$) prepared by etching Ti_3AlCN MAX precursors with $NiCl_2$, can reach an ultra-low detection limit even at room temperature [196]. The loss of aluminum (Al) atoms during the following annealing process provides anchor points for the doping of Ni atoms. The Ni SA obtained by this method is distributed homogeneously on the support (figure 13(f)). Compared with the Ni(SA)/Ti_3CNT_x and Ti_3CNT_x, the Ni(SA)/$TiN_{0.5}C_{0.5}$ showed a much higher response to NO_2 (figure 13(g)). This can be ascribed to the increased presence of defects, including edges and corners, in Ni(SA)/$C_{0.5}N_{0.5}$. This characteristic typically enhances the sensor response to target gases. Notably, the excellent performance of Ni(SA)/Ti_3CNT_x stems from the synergistic effect of Ni atoms and their adjacent Ti atoms. The DFT calculation results (figure 13(h)) illustrate the adsorption geometries of NO_2 molecule on the perfect $TiN_{0.5}C_{0.5}(200)$ surface and Ni(SA)/$TiN_{0.5}C_{0.5}$ surface, respectively. The charge transferred between the gas molecule and sensing material reached its highest (-2.274e) when the NO_2 molecule adsorbed on Ti atoms of Ni(SA)/$TiN_{0.5}C_{0.5}$, higher than that of perfect $TiN_{0.5}C_{0.5}(200)$ surface (-2.48e) and the Ni atoms of Ni(SA)/$TiN_{0.5}C_{0.5}$ (-2.31e). The corresponding adsorption energy of NO_2 adsorbed on Ti atoms was -2.76 eV, which is the lowest value among these three sensing materials. Therefore, the sensing mechanism Ni(SA)/$TiN_{0.5}C_{0.5}$ to NO_2 can be described as follows. The Ni SAs act as an electron giver to increase the electron density of Ti atoms in their vicinities, which facilitates the electron transfer from the sensitive material Ni(SA)/$TiN_{0.5}C_{0.5}$ to adsorbed NO_2 molecules. Apart from the high response, Ni(SA)/$TiN_{0.5}C_{0.5}$ exhibits exceptionally high selectivity to NO_2 with almost negligible responses to interfering gases such as NH_3, CO and H_2S. According to DFT calculations, the adsorption energy ($0 \sim -1.0$ eV) and electron transfer (<0.4e) between Ni(SA)/$TiN_{0.5}C_{0.5}$ and the interfering gas molecules are significantly lower than those associated with NO_2, thereby contributing to its remarkably high selectivity to NO_2.

5.4. Sulfur dioxide

Sulfur dioxide (SO_2) is a toxic pollutant gas with a substantial adverse impact on the environment and human health. Prolonged exposure to even low concentrations of SO_2 can lead to health issues such as asthma, liver damage, and lung damage. Additionally, buildings can be gradually corroded by SO_2 in the atmosphere. Therefore, the development of highly sensitive, real-time gas sensors is crucial for monitoring its concentration both in outdoor environments and indoors.

An ultra-sensitive SO_2 gas sensor has been fabricated using Ni SA anchored on oxygen vacancy-rich SnO_2 nanorods (Ni(SA)/H-SnO_2) as a sensitive material. After the introduction of Ni SA, the morphology of SnO_2 nanorods remains the same as before (figure 14(a)). The energy dispersive x-ray spectroscopy (EDS) line scan of the material demonstrates a uniform distribution of Ni SA on the nanorods (figure 14(b)) without any segregation or secondary nucleation. The Ni SA modification greatly improves the gas-sensitive properties of the material compared with the initial materials (figures 14(c) and (d)). Evidently, the presence of Ni SA on the SnO_2 surface dramatically enhances the sensitivity of the material, regardless of the presence of oxygen vacancies. However, there exists a coupling effect between the oxygen vacancies on the SnO_2 surface and its nearby Ni single atoms, as revealed by analyzing *in-situ* diffuse reflectance infrared Fourier transform spectroscopy of SO_2 adsorption on Ni(SA)/H-SnO_2. This synergistic effect can promote the adsorption of SO_2 and activate chemisorbed oxygen. On one hand, oxygen vacancies serve as adsorption sites for oxygen gas in the air, where the adsorbed oxygen gas converts into superoxide radicals through electron transfer. On the other hand, the Ni SA serve as adsorption sites for SO_2 molecules by forming Ni–S bonds. The enriched SO_2 and superoxide radicals on the sensitive material surface undergo a reaction, effectively releasing captured electrons by oxygen ions to the conducting bands of SnO_2. Consequently, the synergistic effect of Ni SA and oxygen vacancies significantly enhances sensitivity and improves the detection limit [107].

In the dynamic response curves, the sensor's response is essentially linear with respect to the target gas concentration (figure 14(d)). Moreover, the sensor is capable of detecting SO_2 at concentrations as low as 100 ppb (figure 14(d)). In addition to improving the response, the introduction of Ni SA resulted in improved selectivity for sulfur dioxide (figure 14(e)). The Ni solely boosts the response of the sensing material to

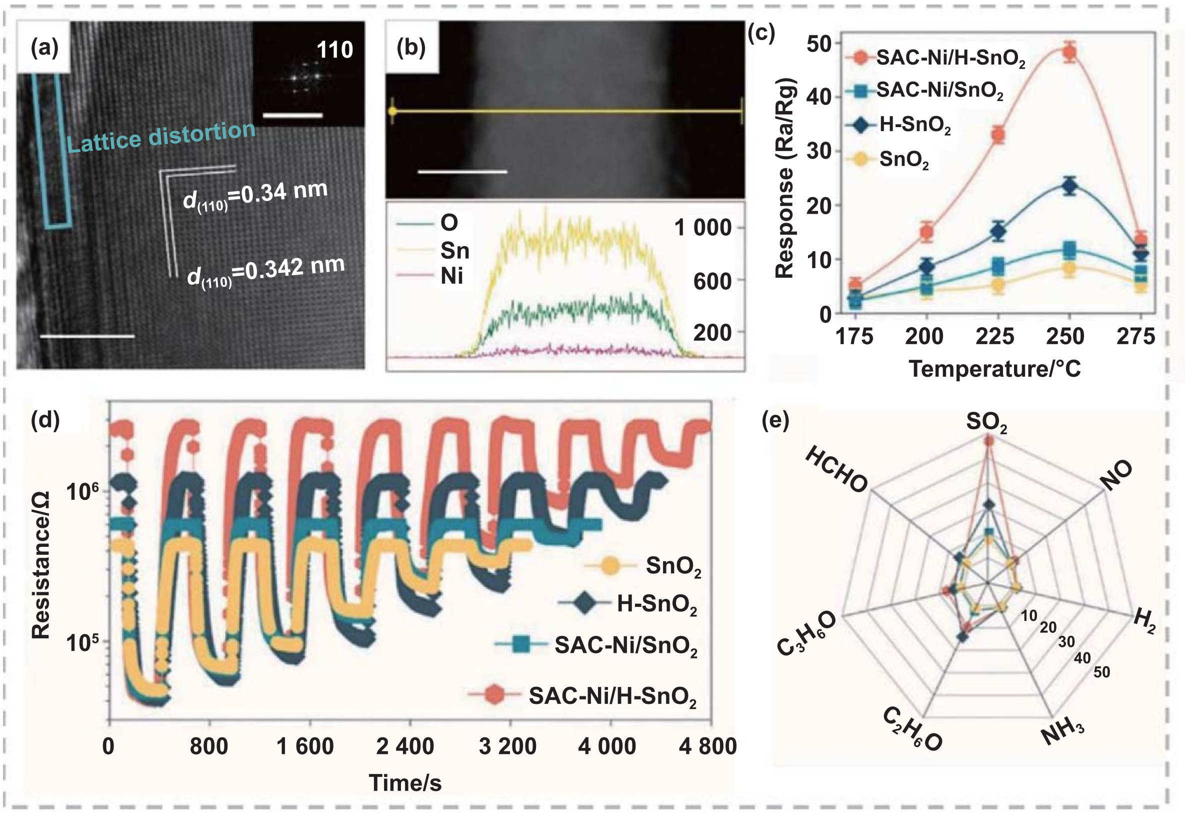

Figure 14. The application of SACs in SO_2 sensing. (a) HRTEM image of Ni(SA)/H-SnO_2, the inset shows the corresponding electronic diffraction spectra (scale bar, 2 nm). (b) STEM-EDS line profile (scale bar, 100 nm) of Ni(SA)/H–SnO_2. (c) Gas sensing response versus operating temperature of four sensors upon exposure to 20 ppm SO_2 at 40% RH. (d) Dynamic resistance curve of four sensors to 40 ppm–0.1 ppm SO_2 gas at 250 °C and 40% RH. (e) Selectivity of the four sensors toward different gases at 250 °C and 40% RH. Reprinted from [107], © 2021 Elsevier B.V. All rights reserved.

SO_2, while the responses to interfering gases such as NO, H_2, and HCHO remain almost unchanged.

5.5. Volatile organic compounds

TEA is an organic amine compound with a strong ammonia odor, widely used in the chemical industry [197]. However, the volatility, flammability, and toxicity of TEA pose significant risks to human life and health. Existing TEA gas sensors face challenges such as long response times, low sensitivity, and unsatisfactory specificity [184]. SACs present a new avenue for designing and developing high-performance TEA sensors. Pt single atoms, in particular, feature a highly reactive surface and excellent stability. The weak bond between the single-atom-sized Pt atoms and oxygen facilitates the participation of surface oxygen in the gas sensing process, which is favorable to increase the content of active oxygen ions (O^{2-}) on the support surface. According to a large number of literature reports, Pt has excellent performance for the detection of TEA [64]. For example, highly selective TEA sensors with Pt SA loaded on 3D ordered macroporous WO_3 (Pt(SA)/WO_3) were prepared by the colloidal crystal template method (figure 15(a)) [79]. The HAADF-STEM image manifests that nearly 80% of the Pt exists as isolated atoms on WO_3 (figure 15(a) right part, red circles). The Pt(SA)/WO_3-based sensor has a high sensitivity of 28.37 ppm^{-1} for TEA with a theoretical detection limit of 0.18 ppb, which exhibits excellent selectivity for TEA compared to other volatile organic compounds (VOCs) and gases (figures 15(b) and (c)). The excellent sensing response is attributed to the atomically dispersed Pt atoms, which increase the number of active sites for adsorbed oxygen and decrease the activation energy. As a result, a significant change in the resistance of Pt(SA)/WO_3 occurs even at low concentrations of TEA. Xu *et al* deposited Pt SA on a SnO_2 film (Pt(SA)/SnO_2) by ALD method as the sensitive material for a TEA sensor [184]. The spillover activation of oxygen by the Pt SACs significantly improved the sensing performance of the SnO_2 film, showing a response of 136.2 for 10 ppm TEA at 200 °C. The detection limit was as low as 7 ppb, accompanied by very fast response and recovery times (3/6 s). This is superior to any previously reported sensors of TEA [198–200]. Apart from the Pt SACs, the atomically dispersed Ag loaded on WO_3 (Ag(SA)/WO_3) can also serve as a sensitive material to achieve efficient detection for TEA. The Ag(SA)/WO_3 obtained by hydrothermal and low-temperature deposition exhibited a low oxidative activation energy and highly sensitive performance

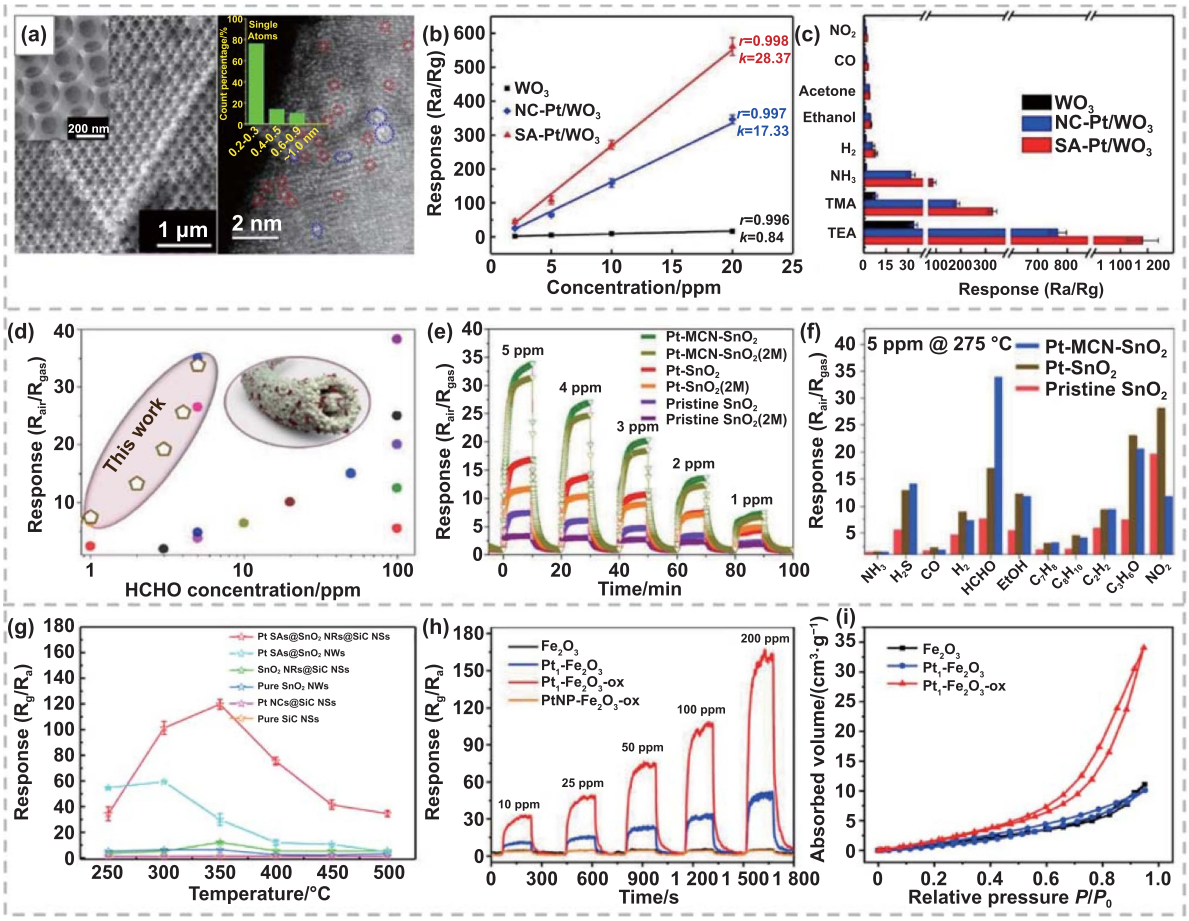

Figure 15. The applications of SACs in VOCs sensing. (a) SEM images (left) and AC-HAADF-STEM image (right) of Pt(SA)/WO_3 (atomically dispersed Pt species and sub-nm clusters are marked with red and blue circles, and the inset is the size distribution based on over 100 Pt species. The inset is a higher magnification SEM image). (b) Response of different sensitive materials to various TEA concentrations. (c) Responses of the Pt(SA)/WO_3 sensors to different gases. Reprinted from [79], © 2019 Elsevier B.V. All rights reserved. (d) Response of state-of-the-art formaldehyde gas sensors compared with that of Pt(SA)/MCN-SnO_2. (e) Long-term stability of Pt(SA)/MCN-SnO_2 in comparison with reference samples; 2 M represents that the sample has been re-evaluated after 2-month-storage on a shelf under an air atmosphere. (f) Selectivity of Pt(SA)/MCN-SnO_2 toward nine different gas species compared with reference samples. Reprinted with permission from [76]. Copyright (2020) American Chemical Society. (g) Gas sensing response towards 500 ppm ethanol versus operating temperature of different sensors. Reprinted with permission from [202]. Copyright (2020) American Chemical Society. (h) Response of the Fe_2O_3, Pt(SA)/Fe_2O_3 and Pt(SA)/Fe_2O_3-ox to C_2H_5OH in concentrations of 10 ppm–200 ppm at 280 °C. (i) Comparative analysis of the C_2H_5OH adsorption–desorption isotherms to the Fe_2O_3, Pt(SA)/Fe_2O_3 and Pt(SA)/Fe_2O_3-ox. Reprinted with permission from [203]. Copyright (2020) American Chemical Society.

for TEA [201]. It demonstrated a high response of 5150 ppm to 50 ppm TEA at 175 °C, a low detection limit of 1.7 ppb, and long-term stability. The excellent performance is mainly attributed to the catalytic and spillover effects of Ag SACs, which increase the number of loaded active sites, lower the energy barrier, and enhance TEA adsorption. In the future, it is anticipated that more kinds of SACs will be developed to realize the advanced sensing performance of TEA.

Formaldehyde (HCHO), as a member of VOCs, finds widespread use in various fields, including medicine, chemical industry, and construction [204]. Unfortunately, due to its colorless, odorless and strong toxicity, it may pose a serious and undetectable threat to human health. Long-term exposure to ppb concentrations of HCHO can cause bronchial asthma, respiratory irritation, and even genetic mutations in humans [205]. Therefore, the development of a highly sensitive HCHO gas sensor is of great significance. SACs with unique advantages have been applied to detect HCHO for years. Atomically dispersed Au was loaded on In_2O_3 nanosheets (Au(SA)/In_2O_3) via a UV-assisted reduction method for highly sensitive and selective detection of HCHO [206]. The Au(SA)/In_2O_3 has a high response (R_{air}/R_{gas} = 85.67) to 50 ppm HCHO at low operating temperatures (100 °C) and an ultra-low detection limit of 1.42 ppb. Meanwhile, the sensor has excellent selectivity for HCHO (100 ppm) at 100 °C [206]. The Au SACs can promote the sensitivity of In_2O_3 by acting as an electron tank, which extracts electrons from the conduction band of In_2O_3 and forms a Schottky barrier at the interface with In_2O_3, increasing the adsorption of oxygen and accelerating the electron transfer process. In addition, Il-Doo Shin *et al* reported a strategy to capture Pt SA on one-dimensional carbon nitride/SnO_2 heterojunctions by electrospinning (Pt(SA)/MCN-SnO_2), yielding maximized catalytic active sites [76]. Meanwhile, the sensing performance of Pt(SA)/MCN-SnO_2 for HCHO is superior to other advanced HCHO gas sensors reported so far (figure 15(d)). Besides the higher response (figure 15(d)) and selectivity (figure 15(f)), Pt(SA)/MCN-SnO_2 exhibits an ultra-high long-term stability in its sensitivity to HCHO. After cyclic exposure to HCHO at 275 °C for 1 week followed by storage on the shelf for 2 months, the sensor response of Pt(SA)/MCN-SnO_2 was found to decrease by only 7.1% (figure 15(e)). This excellent long-term thermal stability results from the dual stabilization of Pt SACs from both MCN and SnO_2. Furthermore, ten different gases commonly found in air at a concentration of 5 ppm were detected by Pt(SA)/MCN-SnO_2. The selectivity of Pt(SA)/MCN-SnO_2 for formaldehyde was significantly enhanced by the doping of Pt SA. This is because that Pt SA may have a catalytic mechanism to enhance the adsorption of HCHO molecules by acting as a binding site for HCHO (figure 15(f)). Recently, Zhang *et al* reported the preparation of Ru(SA)-sensitized SnO_2 nanoparticles as sensors for HCHO detection using ALD method. Ru(SA) significantly increased the adsorption and charge transfer between HCHO molecules and SnO_2. As a result, the response of the Ru(SA)/SnO_2 sensor to 20 ppm HCHO improved by nearly 23 times and the response recovery time was as short as 4 s–29 s [207]. Therefore, SACs hold great promise for formaldehyde detection, as they can achieve high responsivity at low temperatures and maintain long-term stability at high temperatures.

Among VOCs, ethanol(C_2H_5OH) finds extensive use in various industries, including biochemical, food, and transportation industries. Ethanol poses a flammability and potentially explosiveness risk at low concentrations and room temperature. Therefore, controlling ethanol emissions in industrial environments is crucial for both production and human safety. Qiu *et al* first achieved a highly responsive and selective detection of ethanol gas at room temperature using SACs [208]. Atomically dispersed zinc on the nitrogen doped graphene (Zn(SA)/NC_2) was prepared using a two-stage pyrolysis method with a low annealing rate. The Zn(SA)/NC_2 based sensor exhibits a response of 25% to 1 500 ppm C_2H_5OH at 25 °C with excellent selectivity. The DFT calculations showed that C_2H_5OH chemisorbed on Zn(SA)/NC_2 and formed a strong Zn–O bond, resulting in a strong charge transfer between ethanol and Zn(SA)/NC_2. The study demonstrates the great potential of SACs in the detection of ethanol. Moreover, heterojunction catalysts have been constructed to realize high-performance ethanol detection operating under the high-temperature conditions [202]. In detail, the tin oxide nanorods (SnO_2 NRs) and Pt SA were loaded onto silicon carbide nanosheets (SiC NSs) to form a novel Pt(SA)/SnO_2(NRs)-SiC(NSs) multi-heterojunction catalyst. Upon the heterojunction, the highest responsivity is (119.75 ± 3.90) to 500 ppm ethanol at 350 °C, which is much higher compared with that from the pristine SnO_2 and SiC (figure 15(g)). Moreover, the sensor could detect ethanol even at ppb level with a short response/recovery times (~14 s and ~20 s), exhibiting a response of ~1.4 for 500 ppb ethanol at 350 °C. This enhanced sensing performance can be attributed to the effective role of Pt SACs as catalysts, promoting oxygen adsorption and providing a significant amount of ionized oxygen. Additionally, the electronic interactions are effectively enhanced due to the distinct work functions of Pt and SnO_2. Furthermore, the oxidation state and coordination environments of Pt SAs can exhibit completely different reaction and adsorption capabilities, positively impacting the gas-sensitive performance. Li *et al* reported the dispersion of Pt SACs on one-dimensionally aligned porous γ-Fe_2O_3 nanoparticles (Pt(SA)/Fe_2O_3) [203]. After a series of heat treatments at different atmospheres and temperatures, the Pt SAs in the material had different valence states. The results of gas sensitivity tests showed that the Pt(SA)/Fe_2O_3-ox with high-valence Pt has a high response ($R_a/R_g = 102.4$) (figure 15(h)) and good selectivity. This is due to the fact that Pt atoms with high valence can effectively increase the adsorption capacity for ethanol, thereby improving the sensitivity (figure 15(i)). The findings demonstrate the influence of the valence state of SACs on the detection performance of VOCs.

Above all, the SACs-based gas sensors are studied for the detection of different gases (table 2). These sensors exhibit excellent performance, including high sensitivity, low limit of detection, and fast response/recovery. To reveal the sensing mechanism, more powerful techniques such as AC-HAADF-STEM, EXAFS spectra, and *in-situ* spectroscopy are applied, which can give more information about the distribution and electrical structure of target atoms directly [209–211]. At the same time, theoretical calculations such as DFT, can help in selecting the most effective SACs among potential materials, which can provide theoretical guidance for experiments and greatly reduce experimental costs [212–214].

Table 2. Reported SAC-based gas sensors and their performance.

Material	Response	Conc/ppm	LOD/ppb	Operation temperature/°C	Response/recovery time/s	Analytes	References
Co(SA)/ZnO	1.4[a]	0.084	/	200	49/449	O_3	[215]
Au(SA)/ZnO	12.6[b]	0.3	/	150	/	NO_2	[90]
Ni(SA)/H-SnO_2[f]	0.61 ppm^{-1}	0.1 ∼ 40	100	250	52/45	SO_2	[107]
Pd(SA)/Co_3O_4	∼80[b]	1 000	/	125	25/33	H_2	[216]
Pd(SA)/TiO_2	126.92[a]	100	23	RT	27/65	CO	[217]
Co(SA)/N-C	1.34[b]	100	/	RT	780/900	NH_3	[103]
Au(SA)/In_2O_3	3.98[b]	70	/	360	2/10	CO	[218]
Ni(SA)/N_2O_2		0.3 ∼ 180 ppb	/	/	/	NO	[219]
Pt(SA)/$CuCrO_2$	1 250[b]	10	/	100	793/61	H_2S	[89]
Si(SA)/GNs	21.5[a]	50	18	16	126/378	NO_x	[220]
Pd(SA)/In_2O_3	120[b]	10	100	/	100/300	H_2S	[80]
Pt(SA)/B-MoS_2	205%[a]	10	100	RT	25/20	H_2S	[192]
Ni(SA)/$TiC_{0.5}N_{0.5}$	11.2%[a]	0.1	10	RT	/	NO_2	[196]
Pb(SA)/CdSe QD	0.06%/ppb[a]	/	11	RT	29/28	NO_2	[194]
Pt(SA)/$Ti_3C_2T_x$	4%[d]	0.5	14	RT	25/225[c]	TEA	[182]
Pt(SA)/SnO_2	15[b]	10	7	200	3/6	TEA	[184]
Pt(SA)/WO_3	570%[b]	10	0.18	240	20/253	TEA	[79]
Ag(SA)/WO_3	5 150[b]	50	1.7	175	189/1 354	TEA	[201]
Ag(SA)/$LaFeO_3$@ZnO − Pt[g]	21.25[b]	0.062	3.27	86	81/79	Methanol	[181]
Pt(SA)/MCN-SnO_2 [h]	35[b]	5	/	275	/	HCHO	[76]
Au(SA)/In_2O_3	85.67[b]	50	1.42	100	25/198	HCHO	[206]
Zn(SA)/NC_2	25%[a]	1 500	5 000	RT	/	Ethanol	[208]
Pt(SA)/Fe_2O_3-ox[i]	30[b]	10	/	280	30/24	Ethanol	[203]
Pt(SA)/SnO_2 NRs-SiC NSs[j]	119.75[b]	500	500	350	14/20	Ethanol	[202]
Pt(SA)/MoS_2	32%[e]	50	5 000	RT	22/48	Ethanol	[60]

[a] response $= \Delta R/R_a$.
[b] response $= R_a/R_g$ or R_g/R_a.
[c] ambient humidity 20%RH.
[d] response $= \Delta I/I_0$.
[e] response $= \Delta G/G_0$.
[f] Ni SA anchored on oxygen vacancy-rich SnO_2 nanorods.
[g] Pt single atom supported on a porous Ag–LaFeO3@ZnO core–shell sphere.
[h] Pt-MCN (shredded carbon nitride nanosheets)-functionalized tin oxide (SnO_2) nanofiber-in-tube structure.
[i] Pt(SA)/Fe_2O_3 with a further oxidation process.
[j] NR denotes nanorods, NS denotes nanosheets.

6. Summary and perspectives

In summary, this review is focused on the preparation of SACs for various gas sensing via the semiconductor-based electrical sensors. Firstly, the structure and the working principle of semiconductor-based electrical gas sensors are classified and discussed. Subsequently, the preparation strategies of SACs are investigated systematically. Specifically, the loading and distribution of single atoms for each strategy are compared. Following, the interaction between the SACs and the target gas molecules as well as that between SACs and their supports are summarized. This could be attributed to the improved sensitivity and selectivity of SACs-based gas sensors. Finally, the typical applications of SACs in several gas environments are studied in brief.

In the preparation of SACs, two obstacles hinder their widespread use: aggregation and low loading. Moreover, due to the extremely high surface energy of single atoms, some SACs are characterized by poor stability and a tendency to fail at higher temperatures, during the synthesis process, or after a period of operation [120]. These issues are related to the interactions between the single atoms and the support. Weak interactions and unobstructed movement of the single atoms on the surface of the support lead to a tendency to agglomerate and result in low stability of the single atoms. The number of anchoring sites on the supports defines the upper limit of the single-atom loading. To address these issues, several methods can be adopted, which can potentially solve the problems by enhancing the interactions between single atoms and support materials. Firstly, defect engineering can be employed to improve the anchoring on the surface of the support material. This is achieved by manually creating oxygen vacancies, metal vacancies, corner sites, and step sites. So, the atoms around these positions are highly unsaturated, making it more accessible to capture the target metal atoms. Secondly, the doping effect can be employed to modulate the coordination environment of metal SACs. This strategy can increase the coordination number of SACs and enhance the interactions between SACs and their supports, thereby improving the stability of SACs. Additionally, improving the specific surface area helps to increase the number of anchoring sites and the loading of SACs. Specifically, the adoption of engineered structures (e.g. flower-like, hierarchical features, highly porous, etc.) or 2D materials can dramatically increase the specific area of the sensitive materials. Finally, the physical separation of the SACs precursors by the MOF microporous structure can prevent the aggregation of single atoms during the synthesis process.

Currently, SACs offer two main advantages as gas-sensitive materials: a lower detection limit and higher selectivity compared to traditional materials. Studying the principle behind increased selectivity and reduced detection limits will not only enhance understanding of active site effects but also lay a theoretical foundation for the rational design of gas-sensitive materials, potentially reducing experimental costs significantly. In addition, the sensitivity, response speed, linearity and stability of gas sensors are also crucial indicators. In the future, these properties could be improved via the following methods. To enhance sensitivity, one can optimize it by increasing SACs loading, the material's specific surface area, and constructing heterojunctions between different sensing materials. Regarding stability, it primarily relies on the stability of SACs. Therefore, the methods mentioned above to improve the stability of SACs are applicable here as well. To improve response and recovery speed, accelerating the adsorption and desorption of gas molecules can be achieved by optimizing the SACs' operating environment, for instance, through heat and light irradiation [221], providing additional energy for chemical reactions.

Currently, most gas-sensitive materials share similar requirements for the working environment, including high temperature, atmospheric pressure, and oxygen-rich conditions. Nonetheless, specific usage scenarios, such as low-temperature environments, low pressure, or even close-to-vacuum conditions, and oxygen-free environments, impose new requirements on sensitive materials. Therefore, adopting new preparation and application strategies is necessary to expand the application range of gas-sensitive materials based on SACs. In gas detection on the Moon and Mars, the low-temperature and ultralow-pressure environments limit the usage of most currently available sensitive materials due to their very low adsorption energy. The adsorption energy can be further improved by constructing the SACs' coordination environment, with which a chemical reaction can take place. Furthermore, almost all the gas sensors require an oxygen-rich operating environment because that the sensor output relies on the change in electrical resistance of the sensitive material resulting from the chemical reaction between chemisorbed oxygen and the target gas molecules. However, the absence of oxygen in special environments (e.g. on the Moon, Mars) necessitates an oxygen-free sensing mechanism and corresponding sensitive materials. Therefore, new sensitive materials and sensitization mechanisms that operate in oxygen-free environments should be developed. These sensitive materials must selectively trap the target molecules through purely physical interaction and facilitate electron transfer between the sensitive material and the target gas molecules. The physically selective adsorption of NO_2 on SnS_2 serves as a typical example of this new mechanism.

Acknowledgments

This work was supported by the National Key Research and Development Program of China (2022YFB3204700), the National Natural Science Foundation of China (52122513), the Natural Science Foundation of Heilongjiang Province (YQ2021E022), the Natural Science Foundation of Chongqing (2023NSCQ-MSX2286), the Fundamental Research Funds for the Central Universities (HIT.BRET.2021010).

ORCID iD

Jia Zhang https://orcid.org/0000-0003-0943-7543

References

[1] Song H, Liu J, Lu H Y, Chen C and Ba L 2020 High sensitive gas sensor based on vertical graphene field effect transistor *Nanotechnology* **31** 165503
[2] Zhou M L, Chen X H, Zhang L J and Zeng W 2020 High performance novel gas sensor device for site environmental protection using $Ti_{0.5}Sn_{0.5}O_2$ nanomaterials *J. Nanoelectron. Optoelectron.* **15** 1423–8
[3] Zhou J, Li P, Zhang S, Long Y C, Zhou F, Huang Y P, Yang P Y and Bao M H 2003 Zeolite-modified microcantilever gas sensor for indoor air quality control *Sens. Actuators* B **94** 337–42
[4] Matindoust S, Baghaei-Nejad M, Shahrokh Abadi M H, Zou Z and Zheng L R 2016 Food quality and safety monitoring using gas sensor array in intelligent packaging *Sens. Rev.* **36** 169–83
[5] Guo H D, Li X W and Qiu Y B 2020 Comparison of global change at the Earth's three poles using spaceborne Earth observation *Sci. Bull.* **65** 1320–3
[6] Zhang X, Li C L and Li L F 2022 *In situ* detection technology for deep sea extreme environment: research status and strategies *Bull. Chin. Acad. Sci.* **37** 932–8
[7] Wieler R and Heber V S 2003 Noble gas isotopes on the Moon *Space Sci. Rev.* **106** 197–210
[8] Mahaffy P R *et al* 2015 The neutral gas and ion mass spectrometer on the Mars atmosphere and volatile evolution mission *Space Sci. Rev.* **195** 49–73
[9] Liu J, Sun F X, Zhang F, Wang Z, Zhang R, Wang C and Qiu S L 2011 *In situ* growth of continuous thin metal–organic framework film for capacitive humidity sensing *J. Mater. Chem.* **21** 3775–8
[10] Zhou Y, Lin X G, Wang Y, Liu G Q, Zhu X Y, Huang Y K, Guo Y C, Gao C and Zhou M 2017 Study on gas sensing of reduced graphene oxide/ZnO thin film at room temperature *Sens. Actuators* B **240** 870–80
[11] Alfano B, Polichetti T, Mauriello M, Miglietta M L, Ricciardella F, Massera E and Di Francia G 2016 Modulating the sensing properties of graphene through an eco-friendly metal-decoration process *Sens. Actuators* B **222** 1032–42

[12] Zhu Q Q, Gu D, Liu Z, Huang B Y and Li X G 2021 Au-modified 3D SnS_2 nano-flowers for low-temperature NO_2 sensors *Sens. Actuators* B **349** 130775

[13] Li X L, Lou T J, Sun X M and Li Y D 2004 Highly sensitive WO_3 hollow-sphere gas sensors *Inorg. Chem.* **43** 5442–9

[14] Wang X N, Sun X L, Hu P A, Zhang J, Wang L F, Feng W, Lei S B, Yang B and Cao W W 2013 Colorimetric sensor based on self-assembled polydiacetylene/graphene-stacked composite film for vapor-phase volatile organic compounds *Adv. Funct. Mater.* **23** 6044–50

[15] Wang L Y 2020 Metal-organic frameworks for QCM-based gas sensors: a review *Sens. Actuators* A **307** 111984

[16] Vashist S K and Vashist P 2011 Recent advances in quartz crystal microbalance-based sensors *J. Sens.* **2011** 571405

[17] O'Sullivan C K and Guilbault G G 1999 Commercial quartz crystal microbalances—theory and applications *Biosens. Bioelectron.* **14** 663–70

[18] Chang A, Li H Y, Chang I N and Chu Y H 2018 Affinity ionic liquids for chemoselective gas sensing *Molecules* **23** 2380

[19] Li D S, Xie Z H, Qu M J, Zhang Q, Fu Y Q and Xie J 2021 Virtual sensor array based on butterworth-van Dyke equivalent model of QCM for selective detection of volatile organic compounds *ACS Appl. Mater. Interfaces* **13** 47043–51

[20] Tang Y L, Xu X F, Han S B, Cai C, Du H R, Zhu H, Zu X T and Fu Y Q 2020 ZnO-Al_2O_3 nanocomposite as a sensitive layer for high performance surface acoustic wave H_2S gas sensor with enhanced elastic loading effect *Sens. Actuators* B **304** 127395

[21] Tang Y L, Xu X F, Du H R, Zhu H, Li D J, Ao D Y, Guo Y J, Fu Y Q and Zu X T 2020 Cellulose nano-crystals as a sensitive and selective layer for high performance surface acoustic wave HCl gas sensors *Sens. Actuators* A **301** 111792

[22] Li M *et al* 2019 Colloidal quantum dot-based surface acoustic wave sensors for NO_2-sensing behavior *Sens. Actuators* B **287** 241–9

[23] Li H *et al* 2019 Surface acoustic wave NO_2 sensors utilizing colloidal SnS quantum dot thin films *Surf. Coat. Technol.* **362** 78–83

[24] Park W, Park J, Jang J, Lee H, Jeong H, Cho K, Hong S and Lee T 2013 Oxygen environmental and passivation effects on molybdenum disulfide field effect transistors *Nanotechnology* **24** 095202

[25] Fahad H M, Gupta N, Han R, Desai S B and Javey A 2018 Highly sensitive bulk silicon chemical sensors with sub-5 nm thin charge inversion layers *ACS Nano* **12** 2948–54

[26] Hong S, Wu M L, Hong Y, Jeong Y, Jung G, Shin W, Park J, Kim D, Jang D and Lee J H 2021 FET-type gas sensors: a review *Sens. Actuators* B **330** 129240

[27] Wu Z L, Li Z J, Li H, Sun M X, Han S B, Cai C, Shen W Z and Fu Y Q 2019 Ultrafast response/recovery and high selectivity of the H_2S gas sensor based on α-Fe_2O_3 nano-ellipsoids from one-step hydrothermal synthesis *ACS Appl. Mater. Interfaces* **11** 12761–9

[28] Khan A H, Rao M V and Li Q L 2019 Recent advances in electrochemical sensors for detecting toxic gases: NO_2, SO_2 and H_2S *Sensors* **19** 905

[29] Fergus J W 2007 Solid electrolyte based sensors for the measurement of CO and hydrocarbon gases *Sens. Actuators* B **122** 683–93

[30] Dubbe A 2003 Fundamentals of solid state ionic micro gas sensors *Sens. Actuators* B **88** 138–48

[31] Ji H C, Zeng W and Li Y Q 2019 Gas sensing mechanisms of metal oxide semiconductors: a focus review *Nanoscale* **11** 22664–84

[32] Kumar R, Liu X H, Zhang J and Kumar M 2020 Room-temperature gas sensors under photoactivation: from metal oxides to 2D materials *Nano-Micro Lett.* **12** 164

[33] Nikolic M V, Milovanovic V, Vasiljevic Z Z and Stamenkovic Z 2020 Semiconductor gas sensors: materials, technology, design, and application *Sensors* **20** 6694

[34] Penza M, Rossi R, Alvisi M, Signore M A, Cassano G, Dimaio D, Pentassuglia R, Piscopiello E, Serra E and Falconieri M 2009 Characterization of metal-modified and vertically-aligned carbon nanotube films for functionally enhanced gas sensor applications *Thin Solid Films* **517** 6211–6

[35] Bekyarova E, Davis M, Burch T, Itkis M E, Zhao B, Sunshine S and Haddon R C 2004 Chemically functionalized single-walled carbon nanotubes as ammonia sensors *J. Phys. Chem.* B **108** 19717–20

[36] Yin F F, Yue W J, Li Y, Gao S, Zhang C W, Kan H, Niu H S, Wang W X and Guo Y J 2021 Carbon-based nanomaterials for the detection of volatile organic compounds: a review *Carbon* **180** 274–97

[37] Zou Q Q, Liu B and Zhang Y 2023 Design of an array structure for carbon-based field-effect-transistor type gas sensors to accurately identify trace gas species *J. Mater. Chem.* A **11** 15811–20

[38] Zhao Q N, He Z Z, Jiang Y D, Yuan Z, Wu H R, Su C L and Tai H L 2019 Enhanced acetone-sensing properties of PEI thin film by GO-NH_2 functional groups modification at room temperature *Front. Mater.* **5** 82

[39] Nalage S R, Navale S T, Mane R S, Naushad M, Stadlar F J and Patil V B 2015 Preparation of camphor-sulfonic acid doped PPy–NiO hybrid nanocomposite for detection of toxic nitrogen dioxide *Synth. Met.* **209** 426–33

[40] Liu X H, Zheng W, Kumar R, Kumar M and Zhang J 2022 Conducting polymer-based nanostructures for gas sensors *Coord. Chem. Rev.* **462** 214517

[41] Fratoddi I, Venditti I, Cametti C and Russo M V 2015 Chemiresistive polyaniline-based gas sensors: a mini review *Sens. Actuators* B **220** 534–48

[42] Chen X W, Wang S, Su C, Han Y T, Zou C, Zeng M, Hu N T, Su Y J, Zhou Z H and Yang Z 2020 Two-dimensional Cd-doped porous Co_3O_4 nanosheets for enhanced room-temperature NO_2 sensing performance *Sens. Actuators* B **305** 127393

[43] Duan Z H, Zhao Q N, Li C Z, Wang S, Jiang Y D, Zhang Y J, Liu B H and Tai H L 2021 Enhanced positive humidity sensitive behavior of p-reduced graphene oxide decorated with n-WS_2 nanoparticles *Rare Met.* **40** 1762–7

[44] Zheng W, Liu X H, Xie J Y, Lu G C and Zhang J 2021 Emerging van der Waals junctions based on TMDs materials for advanced gas sensors *Coord. Chem. Rev.* **447** 214151

[45] Meng H, Yang W, Ding K, Feng L and Guan Y 2015 Cu_2O nanorods modified by reduced graphene oxide for NH_3 sensing at room temperature *J. Mater. Chem.* A **3** 1174–81

[46] Li E, Cheng Z X, Xu J Q, Pan Q Y, Yu W J and Chu Y L 2009 Indium oxide with novel morphology: synthesis and application in C_2H_5OH gas sensing *Cryst. Growth Des.* **9** 2146–51

[47] Guo Y J *et al* 2013 Characterization and humidity sensing of ZnO/42° YX $LiTaO_3$ Love wave devices with ZnO nanorods *Mater. Res. Bull.* **48** 5058–63

[48] J L Z *et al* 2019 Advances in designs and mechanisms of semiconducting metal oxide nanostructures for high-precision gas sensors operated at room temperature *Mater. Horiz.* **6** 470–506

[49] J L D *et al* 2019 High humidity enhanced surface acoustic wave (SAW) H_2S sensors based on sol–gel CuO films *Sens. Actuators* B **294** 55–61

[50] Li Z J, Huang Y W, Zhang S C, Chen W M, Kuang Z, Ao D Y, Liu W and Fu Y Q 2015 A fast response & recovery H_2S gas sensor based on α-Fe_2O_3 nanoparticles with ppb level detection limit *J. Hazard. Mater.* **300** 167–74

[51] Li Z J, Lin Z J, Wang N N, Huang Y W, Wang J Q, Liu W, Fu Y Q and Wang Z G 2016 Facile synthesis of α-Fe_2O_3 micro-ellipsoids by surfactant-free hydrothermal method for sub-ppm level H_2S detection *Mater. Des.* **110** 532–9

[52] Xu Y S, Ma T T, Zhao Y Q, Zheng L L, Liu X H and Zhang J 2019 Multi-metal functionalized tungsten oxide nanowires enabling ultra-sensitive detection of triethylamine *Sens. Actuators* B **300** 127042

[53] Su P G, Shiu W L and Tsai M S 2015 Flexible humidity sensor based on Au nanoparticles/graphene oxide/thiolated silica sol–gel film *Sens. Actuators* B **216** 467–75

[54] Liu C, Kuang Q, Xie Z X and Zheng L S 2015 The effect of noble metal (Au, Pd and Pt) nanoparticles on the gas sensing performance of SnO_2-based sensors: a case study on the {221} high-index faceted SnO_2 octahedra *CrystEngComm* **17** 6308–13

[55] Mohammad Yusof N, Ibrahim S and Rozali S 2022 Advances on graphene-based gas sensors for acetone detection based on its physical and chemical attributes *J. Mater. Res.* **37** 405–23

[56] Li Q F, Chen W L, Liu W H, Sun M L, Xu M H, Peng H L, Wu H Y, Song S X, Li T H and Tang X H 2022 Highly sensitive graphene ammonia sensor enhanced by concentrated nitric acid treatment *Appl. Surf. Sci.* **586** 152689

[57] Kwon B *et al* 2022 Ultrasensitive N-channel graphene gas sensors by nondestructive molecular doping *ACS Nano* **16** 2176–87

[58] Hizam S M M, Al-Dhahebi A M and Mohamed Saheed M S 2022 Recent advances in graphene-based nanocomposites for ammonia detection *Polymers* **14** 5125

[59] Ao D, Li Z J, Fu Y Q, Tang Y L, Yan S N and Zu X T 2019 Heterostructured NiO/ZnO nanorod arrays with significantly enhanced H_2S sensing performance *Nanomaterials* **9** 900

[60] Liu B Q, Zhu Q, Pan Y H, Huang F T, Tang L Y, Liu C, Cheng Z, Wang P, Ma J and Ding M N 2022 Single-atom tailoring of two-dimensional atomic crystals enables highly efficient detection and pattern recognition of chemical vapors *ACS Sens.* **7** 1533–43

[61] Liu X H, Ma T T, Pinna N and Zhang J 2017 Two-dimensional nanostructured materials for gas sensing *Adv. Funct. Mater.* **27** 1702168

[62] Cho B *et al* 2015 Charge-transfer-based gas sensing using atomic-layer MoS_2 *Sci. Rep.* **5** 8052

[63] Hashtroudi H, Mackinnon I D R and Shafiei M 2020 Emerging 2D hybrid nanomaterials: towards enhanced sensitive and selective conductometric gas sensors at room temperature *J. Mater. Chem.* C **8** 13108–26

[64] Lei G L, Pan H Y, Mei H S, Liu X H, Lu G C, Lou C M, Li Z S and Zhang J 2022 Emerging single atom catalysts in gas sensors *Chem. Soc. Rev.* **51** 7260–80

[65] Chu T S, Rong C, Zhou L, Mao X Y, Zhang B W and Xuan F Z 2023 Progress and perspectives of single-atom catalysts for gas sensing *Adv. Mater.* **35** 2206783

[66] Wei X Q *et al* 2021 Synergistically enhanced single-atomic site Fe by Fe_3C@C for boosted oxygen reduction in neutral electrolyte *Nano Energy* **84** 105840

[67] Wei X Q, Luo X, Wu N N, Gu W L, Lin Y H and Zhu C Z 2021 Recent advances in synergistically enhanced single-atomic site catalysts for boosted oxygen reduction reaction *Nano Energy* **84** 105817

[68] Yan H, Su C L, He J and Chen W 2018 Single-atom catalysts and their applications in organic chemistry *J. Mater. Chem.* A **6** 8793–814

[69] Li W X, Guo Z H, Yang J, Li Y, Sun X L, He H Y, Li S A and Zhang J J 2022 Advanced strategies for stabilizing single-atom catalysts for energy storage and conversion *Electrochem. Energy Rev.* **5** 9

[70] Zhang T J, Walsh A G, Yu J H and Zhang P 2021 Single-atom alloy catalysts: structural analysis, electronic properties and catalytic activities *Chem. Soc. Rev.* **50** 569–88

[71] Chen Y J, Ji S F, Chen C, Peng Q, Wang D S and Li Y D 2018 Single-atom catalysts: synthetic strategies and electrochemical applications *Joule* **2** 1242–64

[72] Li W H, Yang J R, Wang D S and Li Y D 2022 Striding the threshold of an atom era of organic synthesis by single-atom catalysis *Chem* **8** 119–40

[73] Wei X Q *et al* 2023 Tuning the spin state of Fe single atoms by Pd nanoclusters enables robust oxygen reduction with dissociative pathway *Chem* **9** 181–97

[74] Zhang X X, Sun J H, Tang K S, Wang H R, Chen T T, Jiang K S, Zhou T Y, Quan H and Guo R H 2022 Ultralow detection limit and ultrafast response/recovery of the H_2 gas sensor based on Pd-doped rGO/ZnO-SnO_2 from hydrothermal synthesis *Microsyst. Nanoeng.* **8** 67

[75] Zhou M, Jiang Y, Wang G, Wu W J, Chen W X, Yu P, Lin Y Q, Mao J J and Mao L Q 2020 Single-atom Ni-N_4 provides a robust cellular NO sensor *Nat. Commun.* **11** 3188

[76] Shin H *et al* 2020 Single-atom Pt stabilized on one-dimensional nanostructure support *via* carbon nitride/SnO_2 heterojunction trapping *ACS Nano* **14** 11394–405

[77] Wang L B *et al* 2016 Atomic-level insights in optimizing reaction paths for hydroformylation reaction over Rh/CoO single-atom catalyst *Nat. Commun.* **7** 14036

[78] Ou L X, Liu M Y, Zhu L Y, Zhang D W and Lu H L 2022 Recent progress on flexible room-temperature gas sensors based on metal oxide semiconductor *Nano-Micro Lett.* **14** 206

[79] Gu F B, Cui Y Z, Han D M, Hong S, Flytzani-Stephanopoulos M and Wang Z H 2019 Atomically dispersed Pt (II) on WO_3 for highly selective sensing and catalytic oxidation of triethylamine *Appl. Catal.* B **256** 117809

[80] Liu B, Zhang L J, Luo Y Y, Gao L and Duan G T 2021 The dehydrogenation of H-S bond into sulfur species on supported pd single atoms allows highly selective and sensitive hydrogen sulfide detection *Small* **17** 2105643

[81] Chen Y J *et al* 2020 Engineering the atomic interface with single platinum atoms for enhanced photocatalytic hydrogen production *Angew. Chem., Int. Ed.* **59** 1295–301

[82] Li L, Su H Y, Zhou L C, Hu Z X, Li T K, Chen B B, Li H Y and Liu H 2023 Single-atom Ce targeted regulation SnS/SnS_2 heterojunction for sensitive and stable room-temperature ppb-level gas sensor *Biochem. Eng. J.* **472** 144796

[83] Cheng M, Yang L, Li H Y, Bai W, Xiao C and Xie Y 2021 Constructing charge transfer channel between dopants and oxygen vacancies for enhanced visible-light-driven water oxidation *Nano Res.* **14** 3365–71

[84] Xue Z G *et al* 2021 Tailoring unsymmetrical-coordinated atomic site in oxide-supported Pt catalysts for enhanced surface activity and stability *Small* **17** 2101008

[85] Zhao Y F *et al* 2021 Simultaneous oxidative and reductive reactions in one system by atomic design *Nat. Catal.* **4** 134–43

[86] Peng Y, Lu B Z and Chen S W 2018 Carbon-supported single atom catalysts for electrochemical energy conversion and storage *Adv. Mater.* **30** 1801995

[87] Wang N, Sun Q M, Zhang T J, Mayoral A, Li L, Zhou X, Xu J, Zhang P and Yu J H 2021 Impregnating subnanometer metallic nanocatalysts into self-pillared zeolite nanosheets *J. Am. Chem. Soc.* **143** 6905–14

[88] Jiao L and Jiang H L 2019 Metal-organic-framework-based single-atom catalysts for energy applications *Chem* **5** 786–804

[89] Zhang R F, Deng Z, Shi L, Kumar M, Chang J Q, Wang S M, Fang X D, Tong W and Meng G 2022 Pt-anchored $CuCrO_2$ for low-temperature-operating high-performance H_2S chemiresistors *ACS Appl. Mater. Interfaces* **14** 24536–45

[90] Xue Z G *et al* 2020 One-dimensional segregated single Au sites on step-rich ZnO ladder for ultrasensitive NO_2 sensors *Chem* **6** 3364–73

[91] Liu J Y 2017 Catalysis by supported single metal atoms *ACS Catal.* **7** 34–59

[92] Fonseca J and Lu J L 2021 Single-atom catalysts designed and prepared by the atomic layer deposition technique *ACS Catal.* **11** 7018–59

[93] Zhang P, Xiao Y, Zhang J J, Liu B J, Ma X F and Wang Y 2021 Highly sensitive gas sensing platforms based on field effect transistor—a review *Anal. Chim. Acta* **1172** 338575

[94] Eranna G, Joshi B C, Runthala D P and Gupta R P 2004 Oxide materials for development of integrated gas sensors—a comprehensive review *Crit. Rev. Solid State Mater. Sci.* **29** 111–88

[95] Yuan Z, Bariya M, Fahad H M, Wu J B, Han R, Gupta N and Javey A 2020 Trace-level, multi-gas detection for food quality assessment based on decorated silicon transistor arrays *Adv. Mater.* **32** 1908385

[96] Fahad H M *et al* 2017 Room temperature multiplexed gas sensing using chemical-sensitive 3.5-nm-thin silicon transistors *Sci. Adv.* **3** e1602557

[97] Hu P A, Zhang J, Li L, Wang Z L, O'Neill W and Estrela P 2010 Carbon nanostructure-based field-effect transistors for label-free chemical/biological sensors *Sensors* **10** 5133–59

[98] Janata J and Josowicz M 2003 Conducting polymers in electronic chemical sensors *Nat. Mater.* **2** 19–24

[99] Barsan N and Weimar U 2001 Conduction model of metal oxide gas sensors *J. Electroceram.* **7** 143–67

[100] Lundström I, Sundgren H, Winquist F, Eriksson M, Krantz-Rülcker C and Lloydspetz A 2007 Twenty-five years of field effect gas sensor research in Linköping *Sens. Actuators* B **121** 247–62

[101] Eisele I, Doll T and Burgmair M 2001 Low power gas detection with FET sensors *Sens. Actuators* B **78** 19–25

[102] Li Z and Yi J X 2020 Drastically enhanced ammonia sensing of Pt/ZnO ordered porous ultra-thin films *Sens. Actuators* B **317** 128217

[103] Tian R B, Ji P, Luo Z C, Li J M and Sun J H 2021 Room-temperature NH_3 gas sensor based on atomically dispersed Co with a simple structure *New J. Chem.* **45** 10240–7

[104] Bhati V S, Kumar M and Banerjee R 2021 Gas sensing performance of 2D nanomaterials/metal oxide nanocomposites: a review *J. Mater. Chem.* C **9** 8776–808

[105] Majhi S M, Mirzaei A, Kim H W and Kim S S 2021 Reduced graphene oxide (rGO)-loaded metal-oxide nanofiber gas sensors: an overview *Sensors* **21** 1352

[106] Gai L Y, Lai R P, Dong X H, Wu X, Luan Q T, Wang J, Lin H F, Ding W H, Wu G L and Xie W F 2022 Recent advances in ethanol gas sensors based on metal oxide semiconductor heterojunctions *Rare Met.* **41** 1818–42

[107] Liu L Y, Zhou P, Su X Z, Liu Y H, Sun Y H, Yang H B, Fu H Y, Qu X L, Liu S T and Zheng S R 2022 Synergistic Ni single atoms and oxygen vacancies on SnO_2 nanorods toward promoting SO_2 gas sensing *Sens. Actuators* B **351** 130983

[108] Xiao H M, Hou Y C, Guo Y R and Pan Q J 2023 The coupling of graphene, graphitic carbon nitride and cellulose to fabricate zinc oxide-based sensors and their enhanced activity towards air pollutant nitrogen dioxide *Chemosphere* **324** 138325

[109] Tsymbalenko O, Lee S, Lee Y M, Nam Y S, Kim B C, Kim J Y and Lee K B 2023 High-sensitivity NH_3 gas sensor using pristine graphene doped with CuO nanoparticles *Microchim. Acta* **190** 134

[110] Chang S L, Yang M Y, Pang R, Ye L, Wang X C, Cao A Y and Shang Y Y 2022 Intrinsically flexible CNT-TiO_2-interlaced film for NO sensing at room temperature *Appl. Surf. Sci.* **579** 152172

[111] Vu T D, Cong T N, Huu B L, Duc C N and Huu L N 2019 Surface-modified carbon nanotubes for enhanced ammonia gas sensitivity at room temperature *J. Nanosci. Nanotechnol.* **19** 7447–51

[112] Du Z F, Li C C, Li L M, Yu H C, Wang Y G and Wang T H 2011 Ammonia gas detection based on polyaniline nanofibers coated on interdigitated array electrodes *J. Mater. Sci., Mater. Electron.* **22** 418–21

[113] Wu Z Q, Chen X D, Zhu S B, Zhou Z W, Yao Y, Quan W and Liu B 2013 Enhanced sensitivity of ammonia sensor using graphene/polyaniline nanocomposite *Sens. Actuators* B **178** 485–93

[114] Wojkiewicz J L, Bliznyuk V N, Carquigny S, Elkamchi N, Redon N, Lasri T, Pud A A and Reynaud S 2011 Nanostructured polyaniline-based composites for ppb range ammonia sensing *Sens. Actuators* B **160** 1394–403

[115] Pham T, Li G H, Bekyarova E, Itkis M E and Mulchandani A 2019 MoS_2-based optoelectronic gas sensor with sub-parts-per-billion limit of NO_2 gas detection *ACS Nano* **13** 3196–205

[116] Friedman A L, Keith Perkins F, Cobas E, Jernigan G G, Campbell P M, Hanbicki A T and Jonker B T 2014 Chemical vapor sensing of two-dimensional MoS_2 field effect transistor devices *Solid-State Electron.* **101** 2–7

[117] Ma S Q 2015 Gas sensitivity of Cr doped BN sheets *Appl. Mech. Mater.* **799–800** 166–70

[118] Heller I, Janssens A M, Männik J, Minot E D, Lemay S G and Dekker C 2008 Identifying the mechanism of biosensing with carbon nanotube transistors *Nano Lett.* **8** 591–5

[119] Chen T Y, Chen H I, Hsu C S, Huang C C, Chang C F, Chou P C and Liu W C 2012 On an ammonia gas sensor based on a Pt/AlGaN heterostructure field-effect transistor *IEEE Electron Device Lett.* **33** 612–4

[120] Qin R X, Liu P X, Fu G and Zheng N F 2018 Strategies for stabilizing atomically dispersed metal catalysts *Small Methods* **2** 1700286

[121] He G C, Yan M M, Gong H S, Fei H L and Wang S Y 2022 Ultrafast synthetic strategies under extreme heating conditions toward single-atom catalysts *Int. J. Extrem. Manuf.* **4** 032003

[122] Kaiser S K, Fako E, Manzocchi G, Krumeich F, Hauert R, Clark A H, Safonova O V, López N and Pérez-Ramírez J 2020 Nanostructuring unlocks high performance of platinum single-atom catalysts for stable vinyl chloride production *Nat. Catal.* **3** 376–85

[123] Kwon Y, Kim T Y, Kwon G, Yi J and Lee H 2017 Selective activation of methane on single-atom catalyst of rhodium dispersed on zirconia for direct conversion *J. Am. Chem. Soc.* **139** 17694–9

[124] Hai X *et al* 2022 Scalable two-step annealing method for preparing ultra-high-density single-atom catalyst libraries *Nat. Nanotechnol.* **17** 174–81

[125] Zhang Z Q *et al* 2019 The simplest construction of single-site catalysts by the synergism of micropore trapping and nitrogen anchoring *Nat. Commun.* **10** 1657

[126] Yang L, Shi L, Wang D, Lv Y L and Cao D P 2018 Single-atom cobalt electrocatalysts for foldable solid-state Zn-air battery *Nano Energy* **50** 691–8

[127] Sa Y J *et al* 2016 A general approach to preferential formation of active Fe-N$_x$ sites in Fe-N/C electrocatalysts for efficient oxygen reduction reaction *J. Am. Chem. Soc.* **138** 15046–56

[128] Zhao S Y *et al* 2018 One-pot pyrolysis method to fabricate carbon nanotube supported Ni single-atom catalysts with ultrahigh loading *ACS Appl. Energy Mater.* **1** 5286–97

[129] Cheng Y *et al* 2019 Iron single atoms on graphene as nonprecious metal catalysts for high-temperature polymer electrolyte membrane fuel cells *Adv. Sci.* **6** 1802066

[130] Jiang C J, Shang Z Y and Liang X H 2015 Chemoselective transfer hydrogenation of nitroarenes catalyzed by highly dispersed, supported nickel nanoparticles *ACS Catal.* **5** 4814–8

[131] Cheng N C and Sun X L 2017 Single atom catalyst by atomic layer deposition technique *Chin. J. Catal.* **38** 1508–14

[132] Yan H, Cheng H, Yi H, Lin Y, Yao T, Wang C L, Li J J, Wei S Q and Lu J L 2015 Single-atom Pd$_1$/graphene catalyst achieved by atomic layer deposition: remarkable performance in selective hydrogenation of 1, 3-butadiene *J. Am. Chem. Soc.* **137** 10484–7

[133] Shin H, Ko J, Park C, Kim D H, Ahn J, Jang J S, Kim Y H, Cho S H, Baik H and Kim I D 2022 Sacrificial template-assisted synthesis of inorganic nanosheets with high-loading single-atom catalysts: a general approach *Adv. Funct. Mater.* **32** 2110485

[134] Qiao S M, Wang Q, Zhang Q, Huang C H, He G H and Zhang F X 2022 Sacrificial template method to synthesize atomically dispersed Mn atoms on S, N-codoped carbon as a separator modifier for advanced Li–S batteries *ACS Appl. Mater. Interfaces* **14** 42123–33

[135] Sun Q M, Wang N, Zhang T J, Bai R S, Mayoral A, Zhang P, Zhang Q H, Terasaki O and Yu J H 2019 Zeolite-encaged single-atom rhodium catalysts: highly-efficient hydrogen generation and shape-selective tandem hydrogenation of nitroarenes *Angew. Chem., Int. Ed.* **58** 18570–6

[136] Szilágyi P Á, Rogers D M, Zaiser I, Callini E, Turner S, Borgschulte A, Züttel A, Geerlings H, Hirscher M and Dam B 2017 Functionalised metal–organic frameworks: a novel approach to stabilising single metal atoms *J. Mater. Chem.* A **5** 15559–66

[137] Liu S S, Tan J M, Gulec A, Crosby L A, Drake T L, Schweitzer N M, Delferro M, Marks L D, Marks T J and Stair P C 2017 Stabilizing single-atom and small-domain platinum via combining organometallic chemisorption and atomic layer deposition *Organometallics* **36** 818–28

[138] Sun G D *et al* 2018 Breaking the scaling relationship via thermally stable Pt/Cu single atom alloys for catalytic dehydrogenation *Nat. Commun.* **9** 4454

[139] Hu L Z, Wang T, Nie Q Q, Liu J Y, Cui Y P, Zhang K F, Tan Z C and Yu H S 2022 Single Pd atoms anchored graphitic carbon nitride for highly selective and stable photocatalysis of nitric oxide *Carbon* **200** 187–98

[140] Hu D, Wang L, Wang F and Wang J D 2018 Bimetallic Au-Li/SAC catalysts for acetylene hydrochlorination *Catal. Commun.* **115** 45–48

[141] Sarma B B, Jelic J, Neukum D, Doronkin D E, Huang X H, Studt F and Grunwaldt J D 2023 Tracking and understanding dynamics of atoms and clusters of late transition metals with *in-situ* DRIFT and XAS spectroscopy assisted by DFT *J. Phys. Chem.* C **127** 3032–46

[142] Yang J Y *et al* 2022 Modulating the strong metal-support interaction of single-atom catalysts via vicinal structure decoration *Nat. Commun.* **13** 4244

[143] Zhang Y Q, Yang J, Ge R Y, Zhang J J, Cairney J M, Li Y, Zhu M Y, Li S A and Li W X 2022 The effect of coordination environment on the activity and selectivity of single-atom catalysts *Coord. Chem. Rev.* **461** 214493

[144] Chen J Y *et al* 2018 Surface engineering protocol to obtain an atomically dispersed Pt/CeO$_2$ catalyst with high activity and stability for CO oxidation *ACS Sustain. Chem. Eng.* **6** 14054–62

[145] Sietsma J R A, van Dillen A J, de Jongh P E and de Jong K P 2006 Application of ordered mesoporous materials as model supports to study catalyst preparation by impregnation and drying *Stud. Surf. Sci. Catal.* **162** 95–102

[146] Wang L Q, Huang L, Liang F, Liu S M, Wang Y H and Zhang H J 2017 Preparation, characterization and catalytic performance of single-atom catalysts *Chin. J. Catal.* **38** 1528–39

[147] Ding J, Fan M H, Zhong Q and Russell A G 2018 Single-atom silver-manganese nanocatalysts based on atom-economy design for reaction temperature-controlled selective hydrogenation of bioresources-derivable diethyl oxalate to ethyl glycolate and acetaldehyde diethyl acetal *Appl. Catal.* B **232** 348–54

[148] Liu Q and Zhang Z L 2019 Platinum single-atom catalysts: a comparative review towards effective characterization *Catal. Sci. Technol.* **9** 4821–34

[149] Sun L, Cao L R, Su Y, Wang C J, Lin J and Wang X D 2022 Ru$_1$/FeO$_x$ single-atom catalyst with dual active sites for water gas shift reaction without methanation *Appl. Catal.* B **318** 121841

[150] Millet M-M *et al* 2019 Ni single atom catalysts for CO$_2$ activation *J. Am. Chem. Soc.* **141** 2451–61

[151] Zhu Y F, Kong X, Yin J Q, You R, Zhang B, Zheng H Y, Wen X D, Zhu Y L and Li Y W 2017 Covalent-bonding to irreducible SiO$_2$ leads to high-loading and atomically dispersed metal catalysts *J. Catal.* **353** 315–24

[152] Wang Y, Chen L H, Mao Z X, Peng L S, Xiang R, Tang X Y, Deng J H, Wei Z D and Liao Q 2019 Controlled synthesis of single cobalt atom catalysts via a facile one-pot pyrolysis for efficient oxygen reduction and hydrogen evolution reactions *Sci. Bull.* **64** 1095–102

[153] Qi Y F, Li J, Zhang Y Q, Cao Q, Si Y M, Wu Z R, Akram M and Xu X 2021 Novel lignin-based single atom catalysts as peroxymonosulfate activator for pollutants degradation: role of single cobalt and electron transfer pathway *Appl. Catal.* B **286** 119910

[154] Li J X, Chai G D and Wang X W 2023 Atomic layer deposition of thin films: from a chemistry perspective *Int. J. Extrem. Manuf.* **5** 032003

[155] George S M 2010 Atomic layer deposition: an overview *Chem. Rev.* **110** 111–31

[156] Kaden W E, Wu T P, Kunkel W A and Anderson S L 2009 Electronic structure controls reactivity of size-selected Pd clusters adsorbed on TiO$_2$ surfaces *Science* **326** 826–9

[157] Swain S, Altaee A, Saxena M and Samal A K 2022 A comprehensive study on heterogeneous single atom catalysis: current progress, and challenges *Coord. Chem. Rev.* **470** 214710

[158] Liu X, Su Y and Chen R 2023 Atomic-scale engineering of advanced catalytic and energy materials via atomic layer deposition for eco-friendly vehicles *Int. J. Extrem. Manuf.* **5** 022005

[159] Pan H Y, Zhou L H, Zheng W, Liu X H, Zhang J and Pinna N 2023 Atomic layer deposition to heterostructures for application in gas sensors *Int. J. Extrem. Manuf.* **5** 022008

[160] Oviroh P O, Akbarzadeh R, Pan D Q, Coetzee R A M and Jen T C 2019 New development of atomic layer deposition: processes, methods and applications *Sci. Technol. Adv. Mater.* **20** 465–96

[161] Cheng N C, Shao Y Y, Liu J and Sun X L 2016 Electrocatalysts by atomic layer deposition for fuel cell applications *Nano Energy* **29** 220–42

[162] Cheng N C *et al* 2016 Platinum single-atom and cluster catalysis of the hydrogen evolution reaction *Nat. Commun.* **7** 13638

[163] Sun S H *et al* 2013 Single-atom catalysis using Pt/graphene achieved through atomic layer deposition *Sci. Rep.* **3** 1775

[164] Song Z X *et al* 2020 Engineering the low coordinated Pt single atom to achieve the superior electrocatalytic performance toward oxygen reduction *Small* **16** 2003096

[165] Shi X X *et al* 2020 Copper catalysts in semihydrogenation of acetylene: from single atoms to nanoparticles *ACS Catal.* **10** 3495–504

[166] Yin P Q *et al* 2016 Single cobalt atoms with precise N-coordination as superior oxygen reduction reaction catalysts *Angew. Chem., Int. Ed.* **55** 10800–5

[167] Chen Y J *et al* 2017 Isolated single iron atoms anchored on N-doped porous carbon as an efficient electrocatalyst for the oxygen reduction reaction *Angew. Chem., Int. Ed.* **56** 6937–41

[168] Guo S L, Zhao Y K, Wang C X, Jiang H Q and Cheng G J 2020 A single-atomic noble metal enclosed defective MOF via cryogenic UV photoreduction for CO oxidation with ultrahigh efficiency and stability *ACS Appl. Mater. Interfaces* **12** 26068–75

[169] Jiao L, Wan G, Zhang R, Zhou H, Yu S H and Jiang H L 2018 From metal-organic frameworks to single-atom fe implanted N-doped porous carbons: efficient oxygen reduction in both alkaline and acidic media *Angew. Chem., Int. Ed.* **57** 8525–9

[170] Liu Q *et al* 2022 Presentation of gas-phase-reactant-accessible single-rhodium-atom catalysts for CO oxidation, *via* MOF confinement of an Anderson polyoxometalate *J. Mater. Chem.* A **10** 18226–34

[171] Wu N N *et al* 2022 Atomically dispersed Ru_3 site catalysts for electrochemical sensing of small molecules *Biosens. Bioelectron.* **216** 114609

[172] Yang S T, Liu X L, Niu F Q, Wang L Y, Su K K, Liu W F, Dong H Y, Yue H Y and Yin Y H 2022 2D single-atom Fe–N–C catalyst derived from a layered complex as an oxygen reduction catalyst for PEMFCs *ACS Appl. Energy Mater.* **5** 8791–9

[173] Yuan C Z, Zhan L Y, Liu S J, Chen F, Lin H J, Wu X L and Chen J R 2020 Semi-sacrificial template synthesis of single-atom Ni sites supported on hollow carbon nanospheres for efficient and stable electrochemical CO_2 reduction *Inorg. Chem. Front.* **7** 1719–25

[174] Hou Y, Liang Y L, Shi P C, Huang Y B and Cao R 2020 Atomically dispersed Ni species on N-doped carbon nanotubes for electroreduction of CO_2 with nearly 100% CO selectivity *Appl. Catal.* B **271** 118929

[175] Zhang L K *et al* 2020 Atomically dispersed Co catalyst for efficient hydrodeoxygenation of lignin-derived species and hydrogenation of nitroaromatics *ACS Catal.* **10** 8672–82

[176] Qiu L M, Shen S W, Ma C, Lv C M, Guo X, Jiang H L, Liu Z, Qiao W M, Ling L C and Wang J T 2022 Controllable fabrication of atomic dispersed low-coordination nickel-nitrogen sites for highly efficient electrocatalytic CO_2 reduction *Biochem. Eng. J.* **440** 135956

[177] Li X *et al* 2022 Functional CeO_x nanoglues for robust atomically dispersed catalysts *Nature* **611** 284–8

[178] Han G-F *et al* 2022 Abrading bulk metal into single atoms *Nat. Nanotechnol.* **17** 403–7

[179] Lang R *et al* 2019 Non defect-stabilized thermally stable single-atom catalyst *Nat. Commun.* **10** 234

[180] Nakate U T, Bulakhe R N, Lokhande C D and Kale S N 2016 Au sensitized ZnO nanorods for enhanced liquefied petroleum gas sensing properties *Appl. Surf. Sci.* **371** 224–30

[181] Rong Q, Xiao B, Zeng J Y, Yu R H, Zi B Y, Zhang G L, Zhu Z Q, Zhang J, Wu J S and Liu Q J 2022 Pt single atom-induced activation energy and adsorption enhancement for an ultrasensitive ppb-level methanol gas sensor *ACS Sens.* **7** 199–206

[182] Zong B Y, Xu Q K and Mao S 2022 Single-atom Pt-functionalized $Ti_3C_2T_x$ field-effect transistor for volatile organic compound gas detection *ACS Sens.* **7** 1874–82

[183] Cong W H, Song P, Zhang Y, Yang S, Liu W F, Zhang T Y, Zhou J D, Wang M L and Liu X G 2022 Supramolecular confinement pyrolysis to carbon-supported Mo nanostructures spanning four scales for hydroquinone determination *J. Hazard. Mater.* **437** 129327

[184] Xu Y S, Zheng W, Liu X H, Zhang L Q, Zheng L L, Yang C, Pinna N and Zhang J 2020 Platinum single atoms on tin oxide ultrathin films for extremely sensitive gas detection *Mater. Horiz.* **7** 1519–27

[185] Ma J H, Ren Y, Zhou X R, Liu L L, Zhu Y H, Cheng X W, Xu P C, Li X X, Deng Y H and Zhao D Y 2018 Pt nanoparticles sensitized ordered mesoporous WO_3 semiconductor: gas sensing performance and mechanism study *Adv. Funct. Mater.* **28** 1705268

[186] Niu W J, He J Z, Gu B N, Liu M C and Chueh Y L 2021 Opportunities and challenges in precise synthesis of transition metal single-atom supported by 2D materials as catalysts toward oxygen reduction reaction *Adv. Funct. Mater.* **31** 2103558

[187] Akri M *et al* 2019 Atomically dispersed nickel as coke-resistant active sites for methane dry reforming *Nat. Commun.* **10** 5181

[188] Zhang J, Hu P A, Zhang R F, Wang X N, Yang B, Cao W W, Li Y B, He X D, Wang Z L and O'Neill W 2012 Soft-lithographic processed soluble micropatterns of reduced graphene oxide for wafer-scale thin film transistors and gas sensors *J. Mater. Chem.* **22** 714–8

[189] Trabelsi A B, Alkallas F H, Manthrammel M A, Shkir M and AlFaify S 2022 Improvement in ammonia gas sensing properties of Co doped MoO_3 thin films prepared by cost effective nebulizer spray pyrolysis method *Results Phys.* **43** 106036

[190] Sharma B and Myung J 2019 Pd-based ternary alloys used for gas sensing applications: a review *Int. J. Hydrog. Energy* **44** 30499–510

[191] Li Z J, Yan S N, Wu Z L, Li H, Wang J Q, Shen W Z, Wang Z G and Fu Y Q 2018 Hydrogen gas sensor based on mesoporous In_2O_3 with fast response/recovery and ppb level detection limit *Int. J. Hydrog. Energy* **43** 22746–55

[192] Xue Z G, Wang C, Tong Y J, Yan M Y, Zhang J W, Han X, Hong X, Li Y F and Wu Y E 2022 Strain-assisted single Pt sites on high-curvature MoS_2 surface for ultrasensitive H_2S sensing *CCS Chem.* **4** 3842–51

[193] Guarnieri M and Balmes J R 2014 Outdoor air pollution and asthma *Lancet* **383** 1581–92

[194] Geng X *et al* 2021 Atomically dispersed Pb ionic sites in PbCdSe quantum dot gels enhance room-temperature NO_2 sensing *Nat. Commun.* **12** 4895

[195] Wang C Y, Xie J Y, Chang X, Zheng W, Zhang J and Liu X H 2023 ZnO single nanowire gas sensor: a platform to

investigate the sensitization of Pt *Biochem. Eng. J.* **473** 145481

[196] Chen W M, Li P P, Yu J, Cui P X, Yu X H, Song W G and Cao C Y 2022 *In-situ* doping nickel single atoms in two-dimensional MXenes analogue support for room temperature NO_2 sensing *Nano Res.* **15** 9544–53

[197] Wang H, Luo Y Y, Li K, Liu B, Gao L and Duan G T 2022 Porous α-Fe_2O_3 gas sensor with instantaneous attenuated response toward triethylamine and its reaction kinetics *Biochem. Eng. J.* **427** 131631

[198] Li D K, Li Y W, Wang X H, Sun G, Cao J L and Wang Y 2022 Improved TEA sensitivity and selectivity of In_2O_3 porous nanospheres by modification with Ag nanoparticles *Nanomaterials* **12** 1532

[199] Peng R Q, Li Y Y, Liu T, Si P C, Feng J K, Suhr J and Ci L 2020 Boron-doped graphene coated Au@SnO_2 for high-performance triethylamine gas detection *Mater. Chem. Phys.* **239** 121961

[200] Ju D X, Xu H Y, Xu Q, Gong H B, Qiu Z W, Guo J, Zhang J and Cao B Q 2015 High triethylamine-sensing properties of NiO/SnO_2 hollow sphere P-N heterojunction sensors *Sens. Actuators* B **215** 39–44

[201] Zeng Z J *et al* 2021 Single-atom silver loaded on tungsten oxide with oxygen vacancies for high performance triethylamine gas sensors *J. Mater. Chem.* A **9** 8704–10

[202] Sun L, Wang B and Wang Y 2020 High-temperature gas sensor based on novel Pt single atoms@SnO_2 nanorods@SiC nanosheets multi-heterojunctions *ACS Appl. Mater. Interfaces* **12** 21808–17

[203] Li Q H *et al* 2021 Porous γ-Fe_2O_3 nanoparticle decorated with atomically dispersed platinum: study on atomic site structural change and gas sensor activity evolution *Nano Res.* **14** 1435–42

[204] Yang Z, Cao W, Peng C, Wang T, Li B, Ma H, Su Y, Zhou Z, Yang J and Zeng M 2021 Construction, application and verification of a novel formaldehyde gas sensor system based on Ni-doped SnO_2 nanoparticles *IEEE Sens. J.* **21** 11023–30

[205] Lou C M, Lei G L, Liu X H, Xie J Y, Li Z S, Zheng W, Goel N, Kumar M and Zhang J 2022 Design and optimization strategies of metal oxide semiconductor nanostructures for advanced formaldehyde sensors *Coord. Chem. Rev.* **452** 214280

[206] Gu F G, Di M Y, Han D M, Hong S and Wang Z H 2020 Atomically dispersed Au on In_2O_3 nanosheets for highly sensitive and selective detection of formaldehyde *ACS Sens.* **5** 2611–9

[207] Zhou L H, Chang X, Zheng W, Liu X H and Zhang J 2023 Single atom Rh-sensitized SnO_2 via atomic layer deposition for efficient formaldehyde detection *Biochem. Eng. J.* **475** 146300

[208] Qiu J W, Hu X F, Shi L, Fan J L, Min X J, Zhang W and Wang J L 2021 Enabling selective, room-temperature gas detection using atomically dispersed Zn *Sens. Actuators* B **329** 129221

[209] McCoy D E, Feo T, Harvey T A and Prum R O 2018 Structural absorption by barbule microstructures of super black bird of paradise feathers *Nat. Commun.* **9** 1

[210] Duchesne P N *et al* 2018 Golden single-atomic-site platinum electrocatalysts *Nat. Mater.* **17** 1033–9

[211] Yao Y C *et al* 2019 Engineering the electronic structure of single atom Ru sites via compressive strain boosts acidic water oxidation electrocatalysis *Nat. Catal.* **2** 304–13

[212] Duan K, Li W, Zhu C, Li J Z, Xu J and Wang X F 2022 Promoting sensitivity and selectivity of NO_2 gas sensor based on (P, N)-doped single-layer WSe_2: a first principles study *Results Phys.* **34** 105296

[213] Xu Z W, Shi Z Z, Wang M Y, Song R F, Zhang X Z, Liu G W and Qiao G J 2021 Gas sensing properties of defective tellurene on the nitrogen oxides: a first-principles study *Sens Actuators* A **328** 112766

[214] Mu L, Chen D C and Cui H 2022 Single Pd atom embedded Janus HfSeTe as promising sensor for dissolved gas detection in transformer oil: a density functional theory study *Surf. Interfaces* **35** 102398

[215] Catto A C, da Silva L F, Bernardi M I B, Bernardini S, Aguir K, Longo E and Mastelaro V R 2016 Local structure and surface properties of $Co_xZn_{1-x}O$ thin films for ozone gas sensing *ACS Appl. Mater. Interfaces* **8** 26066–72

[216] Koga K 2020 Electronic and catalytic effects of single-atom Pd additives on the hydrogen sensing properties of Co_3O_4 nanoparticle films *ACS Appl. Mater. Interfaces* **12** 20806–23

[217] Ye X L, Lin S J, Zhang J W, Jiang H J, Cao L A, Wen Y Y, Yao M S, Li W H, Wang G E and Xu G 2021 Boosting room temperature sensing performances by atomically dispersed pd stabilized via surface coordination *ACS Sens.* **6** 1103–10

[218] Li D K, Li Y W, Wang X H, Sun G, Cao J L and Wang Y 2023 Surface modification of In_2O_3 porous nanospheres with Au single atoms for ultrafast and highly sensitive detection of CO *Appl. Surf. Sci.* **613** 155987

[219] Zhou W, Tan Y, Ma J, Wang X, Yang L, Li Z, Liu C C, Wu H, Sun L and Deng W Q 2022 Ultrasensitive NO sensor based on a nickel single-atom electrocatalyst for preliminary screening of COVID-19 *ACS Sens.* **7** 3422–9

[220] Niu F, Shao Z W, Gao H, Tao L M and Ding Y 2021 Si-doped graphene nanosheets for NO_x gas sensing *Sens. Actuators* B **328** 129005

[221] Zhang J, Zhao C, Hu P A, Fu Y Q, Wang Z L, Cao W W, Yang B and Placido F 2013 A UV light enhanced TiO_2/graphene device for oxygen sensing at room temperature *RSC Adv.* **3** 22185–90